NOVEL MANUFACTURE OF RADIOLOGICAL SOURCES BY STEREOLITHOGRAPHY

A Dissertation
Presented to
The Academic Faculty

by

Steven C. Mellard

In Partial Fulfillment
of the Requirements for the Degree
Master's of Science in Nuclear Engineering in the
Woodruff School of Mechanical Engineering

Georgia Institute of Technology
AUGUST 2019

NOVEL MANUFACTURE OF RADIOLOGICAL SOURCES BY STEREOLITHOGRAPHY

Approved by:

Dr. Steven Biegalski, Advisor
Woodruff School of Mechanical Engineering
Georgia Institute of Technology

Dr. Nolan Hertel
Woodruff School of Mechanical Engineering
Georgia Institute of Technology

Dr. Henry La Pierre
College of Science Chemistry and Biochemistry
Georgia Institute of Technology

Date Approved: 22nd July 2019

ACKNOWLEDGEMENTS

I wish to thank my advisor, Dr. Steven Biegalski for providing me with the opportunity and guidance in my career as an applied physicist. I also wish to thank the other members of the Nuclear and Radiological Engineering department, Dr. Anna Erickson, Dr. Weston Stacey, Dr. Nolan Hertel, Dr. Chris Wang, and Dr. Farzad Rahnema for their mentorship over the years.

My work here was made possible by the contributions of many others. To Mm. Daphne Brown, without her hard work I would not have the resources to finish my work. I'd also like to thank Mm. Glenda Johnson for so patiently guiding my through the labyrinth of paperwork to see my degree complete. I wish to thank Dr. Stephen Lamont from LANL for his conversations with Dr. Biegalski that first sparked this line of research. I'd like to thank Mm Hannah Watkins and Mr. Peyton Maynard for their part in this project.

Secondly, I wish to extend my thanks and gratitude to my friends and family for their continued vigilance and support during my many long years of study. I alone could not have achieved my station without them. Specifically, I thank my brothers Jacob and Jesse, for their council and support, and my mother, Janet, for her thoughtfulness and endless faith.

Above all I want share my special appreciation for Jessica, my bride to be, for the ray of sunshine she has spilled into my life. She is my partner, my love, and my friend.

TABLE OF CONTENTS

LIST OF TABLES

LIST OF FIGURES

LIST OF SYMBOLS AND ABBREVIATIONS

A_o	Initial activity at time zero
$\bar{A}$	Mean activity of testing coupons
$\bar{A}_{geo}$	Theoretical activity of geometric build
$\bar{a}$	Mean specific activity of resin batch
AM	Additive Manufacturing
DD	Deuterium/deuterium
H	Radius normalized length
HPGe	High purity germanium
I	Gamma ray emission intensity
I_E	Energy specific gamma ray emission intensity
IPA	Isopropyl alcohol 90%+ concentration
PMMA	Polymethyl methacrylate
MCA	Multi-channel Analyzer
MMA_R	Methyl methacrylic radical
$\bar{m}$	Mean mass of testing coupons
m_s	Sample mass
m_x	Matrix mass
m_{geo}	Mass of the geometric build
m_{powd}	Mass of gold powder
m_{wet}	Wet mass of vial
m_{dry}	Dry mass of vial
m_{empt}	Emptied mass of vial

N	Total number counts detected
N_E	Counts detected under a photopeak centred on E
STL	Stereolithography
STD	Standard deviation
S_o^2	The normalized variance of a mixture before stirring
S_R^2	The normalized variance initial variance
S^2	Mass normalized variance of a single sample
t	time
U_{spec}	Statistical uncertainty of the specific activity
t_c	Counting time
ε	Peak detection efficiency
ε_{geo}	Geometric efficiency
ε_{int}	Intrinsic efficiency
λ	Decay constant
$\sigma_{\bar{A}}$	Standard deviation of the sample activity
$\sigma_{\bar{m}}$	Standard deviation of the sample mass
$\sigma_{\bar{a}}$	Standard deviation of the specific activity
$\bar{\sigma}_{geo}$	Theoretical standard deviation
ρ	Radius normalized distance
φ	Phase volume vol/vol
Ω	Solid angle

SUMMARY

In this work, a method for creating radioactive sources using additive manufacturing is considered. The work includes an overview of the theories a practice of stereolithographic printing as well as an in-depth study of the materials and manufacture of radioactive sources using standard and elastic resins. Various mixing techniques are used and compared. A number of tests were conducted to determine the homogeneity and radiological properties of the mixed resins. Consideration was given to the environmental effects of the sources.

CHAPTER 1. INTRODUCTION

Today the manufacturing industry is in the middle of a renaissance. In the 21st century rapid prototyping and stereolithographic manufacturing technologies created in the 1980's have come into their own. Where once these machines required great volumes of resin they now have shrunk down to a more accommodating size for experimentation. Massive leaps in computing power, and a lapse in patents (Hull 1984), have paved the way for desktop sized machines capable of crafting small yet complex objects of cured resin in a matter of hours (The Ultimate Guide to Stereolithographic 3D printing 2018). New applications for additive manufacturing, including UV stereolithography, are being considered and probed by researchers around the world (Ngo, et al. 2018). Desktop UV stereolithography can create custom formed and fitted products from jewelry and household goods to biomedical and dental appliances at a fraction of the formal cost of industrialized printing systems. The properties of the resins used in these processes vary greatly depending on the final form and function of the prints. Some resins cure with durometers as low as 50A, giving the printed part elastic qualities similar to silicone in nature. Other resins have ceramics mixed into the photoreactive polymer to create a full ceramic 3D printed part after a pyro-process bakes away the polymer matrix. Of the many features UV stereolithography possesses, this ability to mix substances into a photoreactive resin and print a component with new qualities is the interest of this work.

Work (Kodama 1981) in the the early 1980's first set foundations for a process to cure a resin layer by layer using a light source. By 1984 Charles Hull submitted a patent for the first practical STL process and started a company called 3D Systems Inc. to

capitalize on the design. Hull further refined the design with a second patent for a STL process that inverted the traditional setup where by the UV laser cures the resin from above to one where it cures the build from below as it adheres to an inverted build platform as seen in Figure 1.

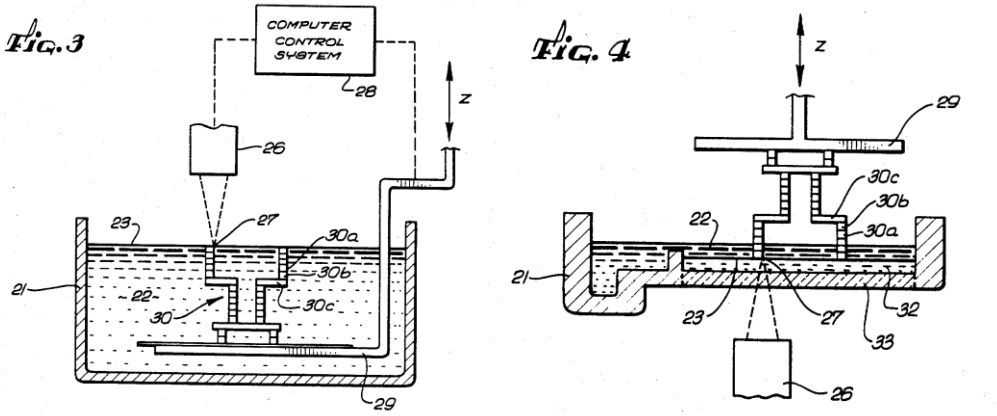

Figure 1 - Artwork from US Patent 4575330 for Apparatus for three-dimensional objects (C. W. Hull 1986) showing the traditional descending method (Left) and the inverted drawing method (Right).

More recently these patents have expired and allowed other companies to compete to create STL systems. Of note is the Formlabs 2 STL printer. Following the modern trend to miniaturize manufacturing technologies this printer can be setup and operated on a surface the size of a desktop. These machines use trays that may be removed and replaced with others, allowing multiple resins to be used on the same machine. The active working volumes of these printers are such that multiple batches may be mixed and tested for efficacy without generating large volumes of waste mixture.

Various groups around the world are currently working to find new and novel ways to include this blooming technology into nuclear and radiological engineering. A particularly active branch of this research is focused on adapting AM techniques to the

manufacture of phantoms for radiotherapy and dosimetry studies. Worked performed at the University of Notre Dame have used bismuth infused ABS (Acrylonitrile butadiene styrene) plastic to emulate the radiopacity of bone tissue in a 3D printed phantom (Ceh, et al. 2017). Efforts from Melbourne, Australia have focused on characterizing the imagery from CT scans of phantom skulls using AM technology (Leary M 2015). Researchers in Malaysia have already used a variety of plastics to print hollow phantoms of pediatric thyroid glands and filled them radiopharmaceutical isotopes to simulate the biological uptake under a CT imager (Alssabbaga, et al. 2017). The work that follows serves to fill out the yet unexplored concept of mixing radiological materials directly into a photoreactive resin and printing sources with variable properties and geometries.

Custom printed designs with varying compositions and quantities of radionuclides have the potential to open up new avenues of study for radiological engineering. Resins doped with radioactive materials could improve capabilities in existing calibration methods and has the potential to create all new ones. For example, an object of complex geometry and unknown radionuclide content might be inspected using a high purity germanium detector. CAD software or a scanning tool may be used to replicate the object digitally as an .STL file in a computer. A replica of the object may then be printed using a homogeneous resin with a known specific activity. The replica could contain a single radionuclide or a combination of several. This replica would then be tested in the germanium detector to provide a result with geometry closely matching that of the original sample. By comparing the results of the photopeaks in the replica to that of the original specimen, inferences can be made to mitigate the changes inaccuracy due to dissimilar geometric efficiency. A physical model may be used to supplement or replace Monte Carlo

computational models as needed. In laboratories without high powered computing resources, computational modeling can take days to complete and may suffer from high levels of uncertainty (Cabal, et al. 2010) as models of the specimen may be printed in a matter of hours, ready for use in calibration and detection. Before the advent of desktop stereolithography this kind of reference material would be costly and impractical to exercise as traditional industrial systems require tens to hundreds of liters of resin. Now, small custom doped batches of resin may be mixed to suit unique applications while minimizing waste.

CHAPTER 2. THEORY

2.1 Overview

Because of the novel nature of the research, the first task was to learn if the creation of 3D printed sources from stereolithography was feasible, and then to determine the properties these sources possess as well as the engineering challenges associated with their manufacture. The radioactive additive needs to be such that its chemistry does not interfere with that of the polymerization process or show considerable degradation in the constitution of the builds. The additive must also uniformly disperse through the liquid resin such a way that the builds have a homogenous mixture of radionuclides in them. The radionuclides may either be added as a powder or dissolved into a matrix before mixing with the resin. Without a consistent specific activity, accurate measurements of HPGe counter sensitivities cannot be made. Other considerations, such as the degradation of plastic over time must be evaluated as well.

To test the homogeneity of the batches several pellet shaped builds with equal dimensions were to be printed. Each would be counted on the germanium detector so that the activity in each pellet might be calculated. With measurement of each pellet's mass, the specific activity of the pellet is simply its activity divided by its mass. The specific activity of the batch as a whole may then be calculated as the average specific activity of the pellets printed. These pellets only represent a sample of the population of possible prints but are assumed to represent the whole.

Once the specific activity of the batch is known, a second set of objects would be printed to test the geometric sensitivities of a HPGe detector. Each build in this new set would be printed simultaneously with others and each would have the same design volume, mass and material as the other builds, but not the same geometry. The concept here being that deviation in the calculated activity greater than which could be accounted from inhomogeneity in the radionuclide dispersion into the resin would be the result of geometric perturbations rather than variations in the concentrations of radionuclides. From these precepts a set of goals have been drafted for research. The following chapter will lay down the foundations of the techniques and science used to critique and analyze the manufacturing methods.

1) Establish a theoretical treatment for mixture analysis sources through literature review.

2) Test combinations of resin and dopants for compatibility. Print test coupons and inspect them for deficiencies or flaws.

3) Print a series of identical pellets from each batch and observe their activities at 411.8 keV using gamma spectrometry. Determine the experimental specific activity and quality of homogeneity in the batches.

4) Print a series of geometric shapes of identical mass and compare their gamma spectrometry results. Identify the geometric efficiency in each shape. Print a complex geometric shape: anatomical heart phantom.

5) Review the printing results and reassess methodology.

2.2 Stereolithography

In brief, stereolithography is a rapid prototyping technology that uses radiation to cure a liquid resin layer upon layer to complete a fully three-dimensional object (Jacobs 1992). Stereolithography was chosen for its high resolution, continuity, isotropy, and ease of doping. Starting off the build platform, a series of skids and scaffolding are built in parallel with the main construction to prevent bending from interfering with subsequent layer. An ultraviolet laser passes in sweeps along the build surface leaving a semi-cured zone between completed layers. Once the build is finished, it's post-cured to fully polymerize the semi-cured layers into a complete whole. The scaffolding is removed and finishing procedures are employed for a polished product.

2.2.1 *Photopolymer Chemistry*

While the exact combination of monomers and oligomers in each Formlabs resin are currently propriety blends, materials safety datasheets provide some information regarding their makeup. Standard resin uses a combination of methacrylate monomers and oligomers are used as the base group and a yet as unidentified photoinitiator as the catalyst. The elastic resin uses a combination of methacrylate oligomers and acylated monomers. A common plastic formed from methacrylate is polymethyl methacrylate (SpecialChem n.d.). PMMA is formed from the methyl methacrylate monomer pictured in Figure 2.

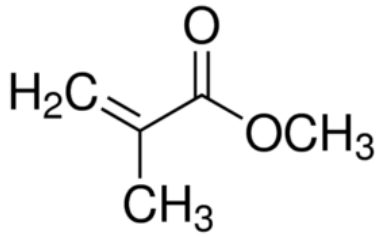

Figure 2 - Chemical structure of methyl methacrylate

PMMA is a tough, transparent thermoplastic with high ultraviolet and chemical resistances. The plastic may be milled, cut, or moulded to shape. It has an optical transparency of 92% and is 100% recyclable (SpecialChem n.d.). PMMA is also easily dyed.

In the polymerization process the resin undergoes three stages initiation, propagation, and termination (Jacobs 1992). Initiation begins when a photoinitiator is converted into a free radical by the absorption of a 405 nm photon. This can be seen in Figure 3 where PI represents the photoinitiator, γ represents the incoming 405 nm photon, and MMA represents either a methyl methacrylic oligomer or monomer. This free radical then bonds to either a monomer or oligomer, radicalizing it. This create a new macroradical then propagates by radicalization and accumulating further monomers and oligomers, as shown in Figure 4. The polymer chain is indicated here by PMMA icon linked to the radicalized methyl methacrylic monomer MMA_R. Additional links are created until the chain in terminated. Termination occurs namely in recombination, when the MMA_R radical encounters another MMA_R or free radical closes the links, or in occlusion when the radicalized polymer chains are trapped by the closed chains around them (Jacobs 1992). Oligomers are groups of monomers already linked together to form short chains of PMMA.

When the photoinitiator is activated these longer chains of MMA allow the resin to cure faster as the monomer come pre-linked.

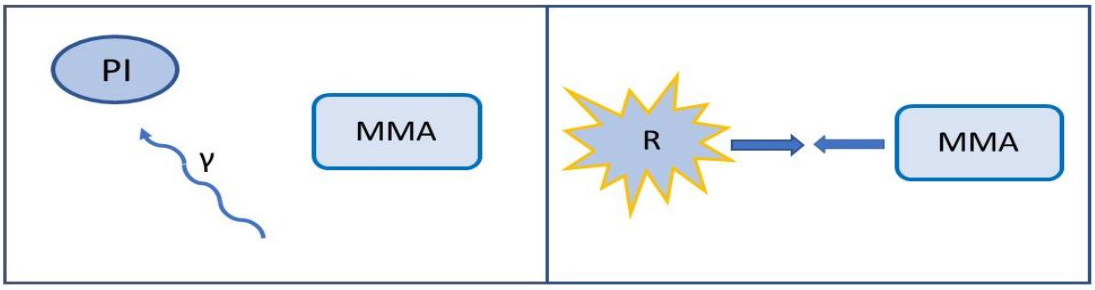

Figure 3- Photoinitiated polymerization of methyl methacrylate.

A feasible additive must either be occluded by the polymerization or become radicalized by the process to be included in the chain through copolymerization or through transfer (Kice 1954). A single photon initiated radical can polymerize upwards of a thousand oligomers and monomers (Jacobs 1992). It is because of this propagation that the radionuclide additive must be chosen so that it does not interfere or otherwise terminate the chain prematurely.

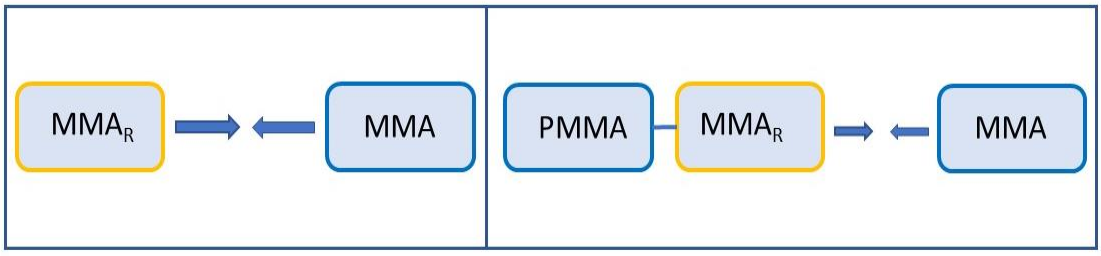

Figure 4 - Propagation of radicalized PMMA molecule.

^{198}Au was chosen for its chemical and radiological properties. With few exceptions, gold is chemically and biologically inert. The ^{198}Au radioisotope decays with a half-life of 2.69 days via a 314.7 keV beta emission. The resulting ^{198}Hg nucleus relaxes within

picoseconds to the ground state by an easily identifiable 411.8 keV gamma ray in 95.62% of these disintegrations. Figure 5 below (Brookhaven Nation Research Laboratory n.d.) shows the decay scheme for ^{198}Au.

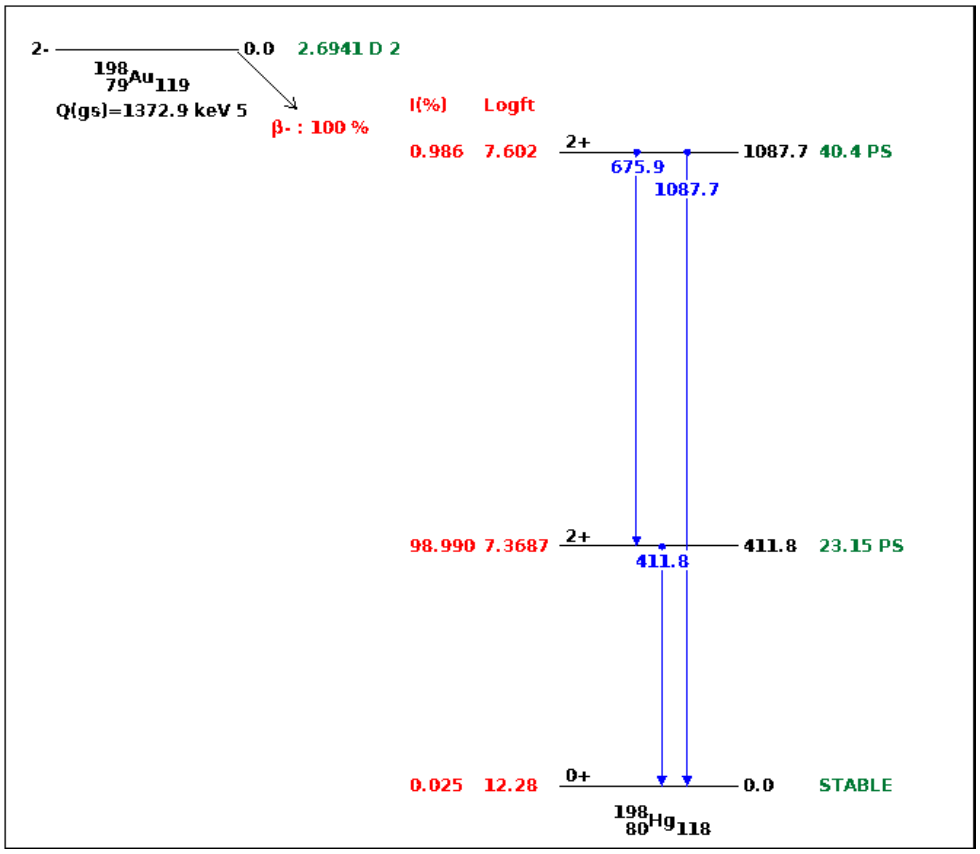

Figure 5 - Decay scheme of ^{198}Au to ^{198}Hg through beta emission. (Courtesy of Brookhaven NuDat database).

Once encapsulated inside resin, the gold continues to decay. The beta emissions are attenuated somewhat by the plastic from self-shielding. The gammas are much less inhibited by the plastic. At 411.8 keV the primary method by which gammas scatter is through Compton scattering. Because the resin is made from low Z materials it lacks the electron density to shield gamma radiation effectively. This was an important factor in determining the radioisotope used. The gold would be radioactive long enough to allow for

printing and spectrographic analysis but would decay quickly enough to avoid long term disposal issues. Gold NIST standards are carefully metered solutions prepared from $AuCl_3$ dissolved in 10% w/w HCl (Inorganic Ventures Inc. n.d.). The result is highly diluted, aqueous chloroauric acid $H^+AuCl_4^-$. The simplest method was to mix the standard directly into the resin without treatment. The second additive considered was activated gold nano powder. The Form 2 printer uses a focused laser beam to sweep a pattern onto the building platform. ^{140}La was selected as an alternate radionuclide for similar reasoning.

2.3 Activity Calculations

2.3.1 *Decay and Activity*

A core feature of this work revolves around calculating the activity of a sample given the number of gamma photons detected in a photo energy peak. The decay of radioactive nuclei follows Equation 1 (Knoll 2010).

$$\frac{A(t)}{A_o} = e^{-\lambda t} \tag{1}$$

Here, $A(t)$ represents the activity at time t where A_o is the activity at $t = 0$, and λ is the decay constant. If original activity is known, then the decay activity may be found at any subsequent time. The relationship between the number of counts detected under the area of the photopeak and the activity of the sample is based on the energy dependant peak efficiency of the detector ε, the number of counts detected, and the intensity of the emitted gamma photon *I*. A correction factor is used for based on the time interval over which the

sample counts were collected t_c, the decay constant of the parent isotope λ, Equation 2 below illustrates the relationship (Nir-El 2013).

$$A(t) = \frac{\lambda N}{\varepsilon I(1 - e^{-\lambda t_c})} \tag{2}$$

In the case of measuring the activity of the calibration source however, the time the samples spent in the HPGe detector was much less than the half-life of the isotopes and consequently $\frac{\lambda}{1-e^{-\lambda t_c}}$ approximates to unity. Another exponential correction factor is used here, one where t may be arbitrarily set to correspond to the time interval *t* between the start of the specimens counting and the end of its irradiation period. Equation 3 may be used to calculate this activity.

$$A_o = \frac{\lambda N}{\varepsilon I e^{-\lambda t}(1 - e^{-\lambda t_c})} \tag{3}$$

In order to benchmark the homogeneity of a batch, the initial activity of each test coupon shall be calculated by the date and time at the end of the batch's irradiation period. The specific activity may then simply become the initial activity of the batch divided by the finished mass of the test coupon. Statistical analysis will then be applied to the results to find the means and standard deviations of the various batches. Theoretical specific activities may be calculated assuming complete homogeneity.

2.3.2 *Detection Efficiency*

In order to determine the geometric efficiency of a source it necessary to remove as many other forms of uncertainty. The total efficiency of the HPGe is the number of detected

photons divided by the number of photons emitted by the source (Knoll 2010). Not all radiation quanta are considered equal and so the efficiency of the HPGe detector is a function of energy. Equation 4 below is valid if the half-life of the radioactive species are much greater than the counting time. Here, N_E represents the number of counts detected under photopeak E in t_c amount of time. $A\,(t)$ may be calculated from Equation 1 and represents the activity of the parent isotope at the start of the count. The intensity of the gamma rays emitted from nucleus I_E depends on the energy of the quanta (Mirion Technologies Inc. 2019).

$$\varepsilon\,(E) = \frac{N_E}{t_c I_E A(t)} \tag{4}$$

By measuring the integrated number of counts under a photopeak and comparing them to the expected counting rate its efficiency may be known. Together with efficiencies from other photopeaks an energy dependent efficiency calibration curve emerges. An n^{th} degree polynomial fitting scheme may be used to relate the efficiency through Equation 5 below (Knoll 2010). Here, C_{n} is the series of coefficients determined from the photopeak data and E is unitless value for energy in keV.

$$\varepsilon = e^{\sum_0^n C_n \ln(E)^n} \tag{5}$$

The peak efficiency of the detector may further categorized as the product of two factors, the intrinsic efficiency and the geometric efficiency, not including small losses from imperfections (Strauss, et al. 1977). The intrinsic efficiency is determined by properties of the detector itself such as the materials it is composed from, the germanium

dead layer, or the energies of the quanta it is registering. Geometric efficiency results more from the shape of the source and its distance from the detector window. In Equation 6, $\frac{\Omega}{4\pi}$ is the geometric efficiency. Ω is a value between 0 and 4π represent the solid angle subtended by the detector surface. (Knoll 2010)

$$\varepsilon_{peak} = \varepsilon_{int} \frac{\Omega}{4\pi} \tag{6}$$

A place circle subtended by the solid angle of a point source may be calculated analytically with simple geometry. However, once the source is presumed to have a volume the analytical calculations for this solid angle become much more complex. Such analytical treatise have been performed for points on a disk(Tyrka 1999) and a cylinder (Guest 1961). It is not the purpose of this work to explore analytical approaches further, but rather to investigate how 3D printing sources might provide an empirical approach to calculating the solid angle or unusual shapes.

To calculate an approximation of the solid angle in the geometric references it will be necessary to find the intrinsic efficiency of the HPGe. For this, Equation 7 below was used from Guest's work (Guest 1961). The multi-gamma standard container was measured by calipers to be 15 mm in length with a 13 mm diameter. The value ρ is the radius normalized distance from the cylinder to the detector surface. *H* is the radius normalized length of the container.

$$\Omega = \frac{2H\left(1+\frac{1}{6\rho^2}\right)}{\rho\left[H^2+\left(\rho-\frac{\pi}{4}-\frac{1}{5\rho}\right)^2\right]^{1/2}} \quad (7)$$

From this evaluation the solid angle used in finding the photopeak efficiency was 0.736 steradians. With the photopeak efficiency from gamma spectrometry, an approximated intrinsic efficiency of the HPGe at 411.8 keV may be determined. From experimental data the geometric efficiencies unique to each geometric shape can be deduced from Equation 6. Intrinsic efficiencies for HPGe's are generally expected to be between 80% and 85% (Strauss, et al. 1977).

2.3.3 *Specific Activity*

To find the specific activity of a batch, Equation 3 and an HPGe detector will be used to find the measured ^{198}Au activity in testing coupons printed from the batch. A digital balance will then be used to find the masses of these coupons. From these data a statistical mean and standard deviation between the coupons may be found for both the activity and mass for each batch. As shown in Equation 8, the specific activity of the batch then becomes the mean activity of the coupons divided by the mean mass.

$$\bar{a} = \frac{\bar{A}}{\bar{m}} \quad (8)$$

2.3.4 *Geometric Evaluation*

Once the specific activity and uncertainty of a batch has been determined they may be used to predict expected values for the activity and standard deviations in the builds of

complex geometry. Six different geometries were used. They were designed in a CAD program with dimensions to give them the same volumes and masses as one another. Once printed the builds will be weighed for mass. The theoretical activity and expected standard deviation are calculated through Equation 9. Here, m_{geo} represents the experimental mass measured, and $\bar{A}_{geo} \pm \bar{\sigma}_{geo}$ are the expected mean activity and standard deviation.

$$\bar{A}_{geo} \pm \bar{\sigma}_{geo} = m_{geo}(\bar{a} \pm U_{spec}) \tag{9}$$

The geometric efficiency may be calculated from the ratio of the predicted net area based on the specific activity of the batch, the measured mass of the sample, and the recorded net area from the germanium detector. This relationship is given in Equation 10.

$$\varepsilon'_{geo} = \varepsilon_{geo} \frac{N_s}{\bar{N}} \tag{10}$$

The geometries are then be counted on the HPGe to produce experimental activities as with the test coupons. Equation 6 is then used to find experimental values for the solid angles of the various geometry. Relative error will be calculated from Equation 11 below to observe how far from the theoretical mean.

$$Err = \frac{(A_{geo} - \bar{A}_{geo})}{\bar{A}_{geo}} \times 100\% \tag{11}$$

Further analysis of the deviation can be made by dividing the build's deviation for the expected mean activity by the expected standard deviation. using the expected standard deviation from Equation 9 as shown in Equation 12. Deviations beyond ± $3\bar{\sigma}_{geo}$ are then

expected to have greater than 99.7% probability from a cause other than inhomogeneity in the batch (Knoll 2010).

$$u = \frac{\left|A_{geo} - \bar{A}_{geo}\right|}{\bar{\sigma}_{geo}} \tag{12}$$

2.4 Homogeneity and Mixing

2.4.1 *Homogeneity calculations*

A statistical approach will be used to quantify homogeneity in the mixtures. This approach was originally meant to describe discrete particle mixing (Lacey 1954), but will be adapted here for use in colloids and emulsions. Assuming complete uniformity, the activity in a random sample of resin can be defined as the matrix activity A times the ratio of the sample mass m_s over the resin mass m_r plus matrix mass m_x. This adjusted value is given in Equation 13. Another important concept is that of the total mass fraction φ in Equation 14. Unfortunately, the physics of mixture homogeneity in a semi-miscible Au/HCl or gold powder matrix in resin is more complicated.

$$\bar{A} = \frac{Am_s}{m_r + m_x} \tag{13}$$

$$\varphi = \frac{m_x}{m_r + m_x} \tag{14}$$

In a colloid or emulsion that activity is quantized in the form of droplets or granules and does not represent a continuum. The amount of activity in a sample rather then becomes a function of the number of particles trapped in resin during the curing of the build. By assuming these particles are distinct from the continuous medium and represent a very small percentage of the mixture mass the variance in the matrix mass of individual samples may be modelled by the Gaussian distribution. One limitation however must be that the dimensions of the sample are much larger than those of the particulates. Here, p represents the probability of finding x number of droplets or granules in the sample and $\bar{x}$ presents the

mean number of particles that are expected in the sample assuming complete uniformity, which is calculated from Equation 15 and the particle volume (Knoll 2010).

$$p(x) = \frac{1}{\sqrt{2\pi\sigma_x}} \exp\left(-\frac{(x-\bar{x})^2}{2\sigma_x}\right) \tag{15}$$

The activity in the sample, and by extension the mass fraction, of the individual measurements are considered gaussian. Consequently, this is helpful because the variances of the activity S^2 are additive. Once the standard deviation of the specific activity is calculated, assertions can be made of the about its accuracy (Ku 1966). If the density and radionuclide concentration of the matrix is assumed homogeneous then the sample mass fraction φ_s can be expressed with Equation 16 and 17. The constant k is the total initial activity divided by the matrix mass.

$$\varphi_s = \frac{kA_s}{m_s} \tag{16}$$

$$k = \begin{cases} \left(\frac{V\rho}{A}\right)_x, HCl\ solution \\ \left(\frac{m}{A}\right)_x, gold\ powder \end{cases} \tag{17}$$

To remain consistent, the matrices measured by volume in the experimental section are converted into mass by the matrix density. The matrix ^{198}Au activity A is a value quoted from University of Texas or calculated from HPGe gamma spectrometry and Equation 3. The variance of the sample from the true value can then be expressed as shown in Equation 18 (Knoll 2010).

$$S^2 = \frac{1}{N-1}\sum_{i=1}^{N}(\varphi_{si} - \varphi)^2 \tag{18}$$

From here two more variances need be identified in order to form the mixing number (Lacey 1954). First of which is the variance found in a completely unstirred mixture S_o^2, and the second for the localized homogeneity inside each sample S_r^2. Equation 19 shows the calculation for an unmixed resin based on mass fraction.

$$S_o^2 = \varphi(1-\varphi) \tag{19}$$

The localized variance S_r^2 is defined as the unmixed mass fraction S_o^2 over the number of particles in sample. In a continuous mixture, the localized variance tends towards zero in very large sample masses as the matrix mass is very small in comparison. In truth however such variances very likely exist but are difficult to determine using gamma spectrometry. Equation 20 provides a ratio of the differences in these variances (Lacey 1954).

$$M = \frac{S_o^2 - S^2}{S_o^2 - S_r^2} \tag{20}$$

M represents the characteristic mixing number. This value is zero when $S_o = S$ and tends towards 1 as *S* goes to zero. Because S_r goes to zero for continuous media the mixing number is better represented in Equation 21 (Berk 2013).

$$M = 1 - \frac{S^2}{S_o^2} \tag{21}$$

2.4.2 *Mixing Physics*

In order to understand the homogeneity of these printed sources it is necessary to understand the fundamentals of mixing on which they are were created. Once the radionuclide's matrix, be it powder or liquid, is added to the resin it exists in its lowest state of homogeneity, that of two separate and distinct masses in contact with one another. Physically this is treated as the introduction of a tracer to the resin, where the mass fraction of the matrix is much smaller than that of the resin. The concentration of radionuclides in the mixture is proportional to the activity by the decay constant. Because there is only a difference by a constant the two will be treated interchangeably. In the case of a liquid matrix, the mixture exists in two phases of liquid. Mixing occurs through emulsification, where the shear forces created by rotation of the impeller impinges on the surface tension of the matrix (Peters 1997). As the process continues, the matrix phase forms droplets which again deform and separate in reaction to the shear forces in the resin. The homogeneity in the mixture then becomes a function of the matrix droplet diameter and their dispersion or diffusion through the resin. This condition is like that of colloid, such as when gold powder is mixed into a resin. Distinct differences should be noted, however. Droplets will be prone to distortion, recombination, and division where granules will not. Additionally, the granule diameter is a result of its manufacture and assumed to be constant whereas droplet volume is a function of mixing conditions such as impeller diameter, rotational velocity and power of that impeller, geometry of the mixing container, and fluid properties of both phases. In both cases however, the droplets or granules are suspended in the resin and can vary in concentration across the volume. While not treated in this work,

the author does recognize that the concentrations will also vary with time (Nienow 1997). The droplets or granules themselves will have a distribution of activity as some are bound to contain more radionuclides than others. Wither by droplet or granule the homogeneity calculations will treat the matrix as particle concentrations inside the resin. From this physical description, a model for homogeneity may be built.

The mass of powder may be calculated from weighing the powder container before, during, and after it is filled using Equation 22. The dry mass m_{dry} is that of the container before the powder is added. The wet mass m_{wet} is the mass of the container with powder and the empty mass m_{empt} it that of the container after the powder had been emptied out.

$$m_x = \left(m_{wet} - m_{dry}\right) - \left(m_{empt} - m_{dry}\right) \tag{22}$$

The number of particles in a powder sample may be estimated by assuming the granules take the form of perfect spheres The volume of a sphere the density of gold (GSU Physics Dept. n.d.), and the average diameter of the gold granules from Appendix B.5 can be used to deduce the number of granules in Equation 23.

$$N_{powd} = \frac{6m_x}{\pi {d_o}^3 \rho} \tag{23}$$

The droplet diameter of the Au/HCl droplets is a more complex calculation. droplet diameter is a function of many variables including the geometry and power input of the impeller and fluid properties of both phases of liquid (Peters 1997). So long as the phase volume φ of the mixture is below 30% the droplets do not collectively interfere with one

another (Peters 1997) and the Gaussian distribution holds. While mentioned here future work will need to apply droplet formation to homogeneity.

2.5 Uncertainty

During experimentation, the true values will be obfuscated by imperfections in the instrumentation. Unlike systematic errors, these imperfections alter the precision of the data. Assuming these sources of error are independent of one another a simple error propagation formula (Knoll 2010) can be used to determine the standard deviation. By using the variance instead of the standard deviation Equation 24 and 25 below represent a linear form.

$$\sigma_u^2 = \left(\frac{\partial u}{\partial x}\right)^2 \sigma_x^2 + \left(\frac{\partial u}{\partial y}\right)^2 \sigma_y^2 + \left(\frac{\partial u}{\partial z}\right)^2 \sigma_z^2 + \cdots \tag{24}$$

$$u = f(x, y, z, \dots) \tag{25}$$

There are two different kinds of uncertainty calculated as part of this work. The first of which is the uncertainty in measurements born out of imprecision in the instruments and the second is the statistical variance between these measurements. Another group of uncertainties are not calculated, but rather quoted from external sources. Examples of these quoted uncertainties are the density of the matrix, the percent error in the number of counts detected by the MCA, or the uncertainties in the volumes dispensed by the pipettes. The statistical means and variance of measurements are then used to find the uncertainty in the specific activities are then used in the error propagation formulas.

The uncertainty in the specific activity of a series of homogeneity samples is found using Equation 8 and Equation 24. Here The uncertainty in the mean mass and mean activity are derived from the statistical definitions of the experimental standard deviation $\sigma_{\bar{A}}$ and $\sigma_{\bar{m}}$ of a sample.

$$\left(\frac{\sigma_{\bar{a}}}{\bar{a}}\right)^2 = \left(\frac{\sigma_{\bar{A}}}{\bar{A}}\right)^2 + \left(\frac{\sigma_{\bar{m}}}{\bar{m}}\right)^2 \tag{26}$$

Similarly, the standard deviation in the mixing number must be calculated from the variance of the mixing number in Equation 27 below. The variances S^2 and S_o^2 of the sample population are simple enough to deduce but finding the related uncertainties σ_S^2 and $\sigma_{S_o}^2$ are more difficult. These require additional applications of the error propagation formula until the uncertainties used are traced back to quoted values from instrumentation.

$$\sigma_M^2 = \frac{4S^2}{S_o^4}\left(\sigma_S^2 + \frac{\sigma_{S_o}^2}{S_o^2}\right) \tag{27}$$

Some uncertainties cannot be determined without data from the experiment. In such cases, such as for σ_N^2, the variance for the value was calculated from the mean variance of several measurements in the sample population. A full list of uncertainties is available in Appendix A.4. Where quoted uncertainties were not available, plus or minus half the value of the readability on the instrument was used. In others, like the resin density, the standard deviation was inferred as plus or minus half the difference of the end of range values. The matrices from the TRIGA reactor did not have accompanying uncertainty data for the quoted activities and were not included. Consequently, the uncertainty in Batch A, B, and F derived from the total activity will be greater than reported.

CHAPTER 3. METHODOLGY

In this chapter, the apparatus, materials, and practice of printing radiological resins will be considered and discussed in detail. Section 3.1 will discuss the printer, form wash, and form curing hardware. Section 3.2 will list the various additional apparatus used in conjunction with the printers to either manufacture radiological or to measure the properties of the prints. Section 3.3 will introduce the materials and Section 3.4 will discuss how the various batches were mixed and stored as well as the procedures used to print and collect data.

3.1 Form 2 Hardware

Figure 6- Form 2 printer (left) Form Wash (center) and Form Cure (right) pictured in the fume hood in the Georgia Tech Forensics Lab.

3.1.1 *Printer Hardware*

The Form 2 Printer from Formlabs came equipped with a resin tray, wiper blade, and build platform. The printer contained a suite of sensors to detect the position of the tray and the build platform. These sensors allowed coordination of the tray, build platform, and a series of rotating mirrors to guide the UV laser in the curing process. The laser had a spot width of 140 μm and cures layers with a resolution between 25 to 300 μm. The build platform was measured to have a 210 cm^2 work area that can support parts with a maximum height of 17.5 cm. During normal operations, an actuator releases resin from a storage container into the printing tray. A heater in the printer auto heats the resin up to 35 °C to promote adhesion in the resin. Once the resin has been warmed to temperature, the build platform descends into the resin, pressing itself against an elastic membrane that separates the tray window from the fluid resin. The UV laser will trace out a pattern for the current prescribed layer. Once complete the build platform will slowly rose from the resin and waited for the tray wiper to clear stray cured resin out of the beam path before resuming the next layer. It is important to note the Form 2 printer had two different modes of operation. The first was the normal mode described above. The second was an open mode for experimentation. In open mode the printer shuts off the wiper, heater, and automatic resin filling features for the tray. In this mode the resin must be periodically hand poured into the tray to refill its contents. The printer was wifi enabled to allow print files and commands to be sent remotely.

3.1.2 *Form Wash Hardware*

The Form Wash hardware consisted of an IPA filled basin with a magnetic impeller fixed at the bottom. The Form Wash also includes a metal wire basket mounted on a motorized lift. The build platform may by placed on the lift to submerge wet builds into the IPA rinse. The Form Wash came with a variety of hand tools used to clean and remove excess scaffolding. A fulcrum was used to release the parts from the build platform and deposit them in the submersion basket. At capacity the basin holds up to 8.6 L of IPA. Users may adjust the temperature of the wash as well as soak time for the parts in question. At the finish of each wash, the lift automatically retracts from the basin so as not to allow the IPA to warp and deform the build. The Form Wash was also equipped with a siphon and hydrometer for maintaining the quality of the IPA bath.

3.1.3 *Form Cure Hardware*

The Form Cure served as a final treatment for build parts. Uncured, green builds were placed underneath the hood of the Form Cure. The machine heated to an internal temperature of between 60 °C and 80 °C while bathing the builds in 405 nm light. This encourages full polymerization of the resin throughout the build. Many of the builds did not meet their full strength or mechanical properties without this additional curing process.

3.2 Additional Hardware

3.2.1 *Mixer*

A Cole-Palmer EW-50006-03 compact digital mixer was used to combine the radionuclides with the resins. The machine can mix up to 2 L of water with a maximum

speed of 2500 rpm at a maximum torque of 1022.51 $g\text{-}cm$. The mixer was fitted with a 30.2 mm impeller. The impeller was cleaned with IPA and shop towels between each batch mixture to avoid contamination.

3.2.2 *Pipettors*

Two Wheaton Socorex Calibra 85340 and 851345 digital pipettors were used to aliquot radiological solutions into the resin. These instruments could dispense between 0.2 mL to 2 mL in 0.01 mL increments for the 851340 unit or 1 mL to 10 mL of liquid in 0.1 mL increments for the 851345 unit. Both pipettors had a prescribed 1.5% uncertainty in the volume dispensed.

3.2.3 *High Precision Balance*

A model ME204TE/00 Mettler Toledo mass balance was used to weigh finished prints after the curing stage. The instrument provided accurate measurements up four decimal places and so was accurate to $\pm 5.0 \times 10^{-5}$ g. The mass balance was purchased less than six months from the time of the experiment and was not yet due for calibration. Glass barriers around the balancing dish reduce error from cross currents.

3.2.4 *High Purity Germanium Detector*

A coaxial Canberra BE3825 HPGe was used with a model 2002CSL preamplifer to perform a gamma spectrographic analysis of all finished builds. The detector sported a copper shield 10 cm in thickness to attenuated background radiation. The detector had quoted resolutions of less than 2.1 keV at 1.33 MeV and less than 0.75 keV at 122 keV. The high purity germanium crystal forms a lattice where the energy gaps between the

electron valence and conduction bands are 2.97 eV per ionization event at 77 K. The detector must be kept cool by liquid nitrogen to reduce signal noise and dark current. Incident gamma rays promote the electrons in this lattice from the valence band to the conduction band while a 4300 V bias current separates the electron hole pairs. These electron hole pairs are detected as minute currents registered by a pre-amplifier. The pre-amp converts the current into voltage peaks which are amplified and sorted by the multi-channel analyser. Genie 2000 spectrographic software was used in conjunction with the detector hardware to calculate values such as the integrated number of counts detected under a peak and the full width half maximum of these peaks. The Genie 2000 software calculates the percent error in the area under the photopeak. Less than 2% error was considered a good approximation.

3.2.5 *Neutron Generator*

A Starfire nGen-800 DD generator was used to activate specimens of lanthanum and gold for use as dopants for the resins. The generator operates as a deuteron accelerator using electrodeless RF ionization to produce fusion reactions that release a 2.5 MeV neutron. The machine could create electric fields up to 180 kV. The high acceleration voltage contributed to a forward biased neutron anisotropy. The machine had a quoted average fluence of $5\times10^{10}\ \frac{neutrons}{s}$ under continuous operation. Without the use of tritium as a resource, the neutron generator contains no significant radioactive materials and only produces radiation when energized. Tritium is generated as a by product of the DD reaction in 50% of the events, but conservative estimates place the activity of such at 140 nCi during 168 operational hours over the course of a year.

3.3 Materials

3.3.1 *^{198}Au Radionuclides*

The ^{198}Au radionuclides used in the experiments were activated from Inorganic Ventures MSAU-10PPM. This solution was composed of 10 ppm gold in a 10% HCl matrix and is a standard traceable to NIST. Inorganic Ventures credits this solution with meeting ISO 17025 and 17034 certifications. Two samples were activated in the General Atomics Mk II TRIGA reactor at the University of Texas Austin. Batch A was a 0.9 mL sample activated at 08:30 on October 16th with a quoted activity of 164 kBq. Batch B was similarly a 0.75 mL sample activated on January 8th 08:30 with a quoted activity of 76.7 kBq. The radionuclides were double encapsulated in a heat-sealed vial for transport. Batch C and D were 1000 ppm gold concentration dissolved in 10% HCl and 1000 ppm lanthanum dissolved in 2% HCl respectively. These batches were produced using a DD neutron activation but resulted in very low activity such that they were not used in printing builds. Batch E consisted of 0.3118 g of spherical gold powder with an average diameter of 1.5 μm from Alfa Aeser, LOT# Z13B025. The details for the powder may be found in Appendix B.5. This gold powder was activated using a DD generator under the same conditions as Batch C and Batch D but resulted in sufficient activity to use in the printing process. Batch F was a 0.6 mL sample of Au and HCl like Batch A and Batch B with a quoted activity of 43980 Bq at 08:30 on May 29th, 2019.

3.3.2 *Multi Gamma Standard*

An Eckert and Zigler certified gamma standard was used to calibrate the HPGe. This standard was produced from E&Z source number 108401A, traced to NIST standards in compliance with ANSI N42.22-1995. The standard was comprised of 10 radionuclides. The reference date used to calculate the decay equations and efficiency calibrations was January 1st 2018, 12:00 PM. Table 1 below contains a listing of trace radionuclides presence in the source.

Table 1 - Eckert and Zeigler Multi-gamma standard for HPGe calibration. Reference date for calibration was 12:00 January 1st , 2018. Intensity data from NuDat (Brookhaven Nation Research Laboratory n.d.).

Radionuclide	Energy (keV)	Half-Life (d)	Activity (Bq)	U (%)	I (%)
^{210}Pb	46.5	8.109×10^{3}	1.450×10^{4}	4.2	4.2
^{241}Am	59.5	1.580×10^{5}	1.162×10^{3}	3.6	35.9
^{109}Cd	88.0	4.614×10^{2}	1.610×10^{4}	4.1	3.6
^{57}Co	132.1	2.717×10^{2}	3.654×10^{2}	3.4	85.6
^{139}Ce	165.9	1.367×10^{2}	5.499×10^{2}	3.6	80.0
^{203}Hg	279.2	4.659×10^{1}	1.185×10^{3}	3.5	81.0
^{113}Sn	391.7	1.151×10^{2}	9.407×10^{2}	3.9	64.0
^{137}Cs	661.7	1.099×10^{4}	4.216×10^{2}	4.1	85.1
^{88}Y	898.0 1836.1	1.066x102	1.577×10^{3}	3.7	93.7
^{60}Co	1173.2 1332.5	1.925×10^{3}	7.219×10^{2}	3.9	99.9

3.3.3 *Photosensitive Resins*

Formlabs provides customers with several commercially available resins to be used with their printer. Standard Formlabs resin came in a variety types. The resins were a mixture of methacrylated polymers, methacrylated oligomers, and photoinitiators. To date, Formlabs keeps the exact compounds and ratios proprietary. Two standard resins were used, clear and pigmented. Both of which bear the same physical properties. These are highlighted in the figure below. Pigmented resins have the benefit of high visibility. In the printing environment, spills and contamination are easier to detect than clear resins. Clear resins on the other hand possess optical properties that may be advantageous in some applications.

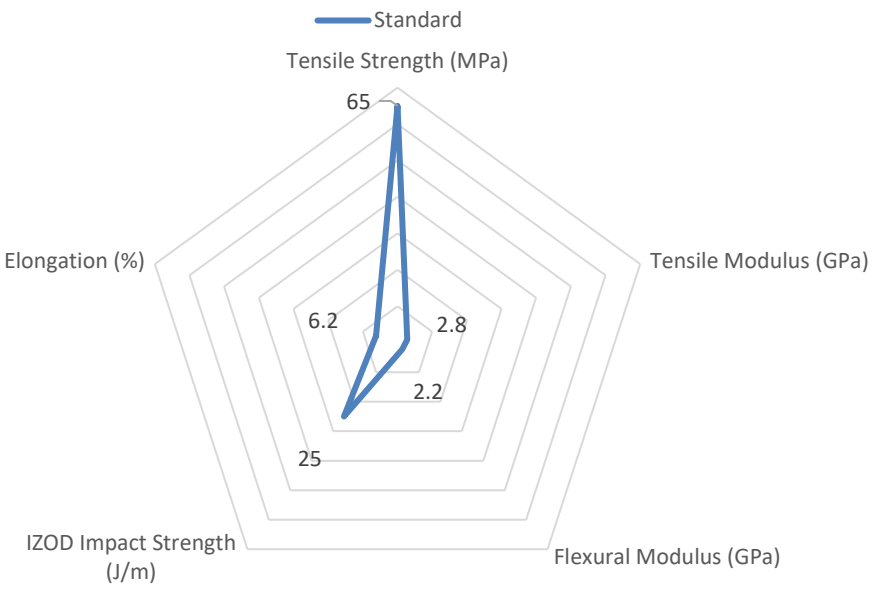

Figure 7- Mechanical properties of Formlabs standard resin. Typical for clear and color bases. See Appendix B.2 for technical data.

The density of the standard resin was quoted by the manufacturer as 1.08 to 1.09 $\frac{g}{cm^3}$ with a viscosity of 8.50 to 9.00 $\frac{g}{cm*s}$, the technical data for which may be found in Appendix B. For calculation purposes, these values were written as 1.0850 ± 0.46% $\frac{g}{cm^3}$ and 8.75 ± 2.8% $\frac{g}{cm*s}$.

The second kind of polymer used in this work was Formlabs elastic resin. The elastic resin was ductile and plastic. It was translucent in nature and resembles silicon in its mechanical properties. Sources printed with this material can stretch, fold, and compress in response to mechanical forces.

3.3.4 *Isopropyl Alcohol (IPA)*

This solvent was procured from LabChem in concentrations over 90%. IPA was used to wash unpolymerized resin off builds. Due to the tendency of the IPA to degrade the integrity of the resin, builds may only be briefly exposed to the substance after the curing process.

3.3.5 *Sodium Bicarbonate*

While not used directly in the printing process, this common alkali compound was kept close at hand in case the radionuclide containing acid matrix were to spill.

3.4 Procedure

3.4.1 *Efficiency Curve Calibration*

The multi-gamma standard was placed on top of a fused deposited PLA cap suspended over the graphene screen of the HGPe detector. The count was taken for one hour to allow a high degree of precision in the efficiency calculation. The raw results from the count were combined with intensity data from NuDat (Brookhaven Nation Research Laboratory n.d.) to calculate the efficiencies at the given energy peaks. The results were fed into a MATLAB program that used Equation 5 to produce the efficiency curve coefficients. An interpolation was made to find the efficiency of the detector at 411.8 keV along with the first order derivative. The MATLAB script may be found in Appendix A.1.

3.4.2 *Batch Test Preparation*

Before radiologicals were used, the effect of mixing HCl acid into clear standard resin was first investigated. The test was made to judge the extent the HCl induced polymerization in the resin.

1. 2 mL of 1 M HCl was dispensed into a graduated borated silica beaker by pipette.
2. Approximately 20 mL of standard clear resin was added to the beaker.
3. The beaker was oscillated to allow the HCl to wash over the resin. A wooden stirring rod was used to fold together the matrix and resin.
4. An additional 220 mL of resin was measured in a separate graduated beaker and poured into the mixing beaker.
5. The mixture was stirred mechanically at 500 rpm for 10 minutes.

3.4.3 *Batch A Preparation*

1. 0.4 mL of ^{198}Au/HCl solution A was aliquoted by digital pipette into a graduated mixing beaker containing approximately 20 mL clear standard resin.
2. The beaker was oscillated by hand to allow the HCl to wash over the resin by rotation of the beak by hand for 30 seconds.
3. A wooden stirring rod was used to fold together the matrix and resin. An additional 180 mL of resin was measure into a separate graduated beaker and poured into the mixing beaker.
4. The mixture was stirred mechanically at 600 rpm for 8 minutes.
5. An additional 0.5 mL of Au/HCl solution A was pipetted into 0.75 mL of water.

6. This diluted solution was poured directly into a beaker containing 200 mL of clear standard resin.
7. This mixture was stirred mechanically at 600 rpm for 6 minutes.
8. The mixtures from 3.4.3 Step 4 and Step 7 were combined together and stirred by hand with a wooden stirring rod for 30 secs.
9. The batch was stored in the mixing beaker until needed.

3.4.4 *Batch B Preparation*

This batch was mixed by adding the radioactive liquid matrix directly to the reservoir of resin. Because the resin remained in its original container it was able to be used with advanced heating and wiping features of the printer.

1. Following manufacturer's directions, 80 mL of cyan pigment, 5 mL of black pigment, and 5 mL of magenta pigment was added by syringe to a Formlabs color base reservoir cartridge with 800 mL of standard resin.
2. The reservoir was resealed and shaken vigorously by hand for 2 minutes.
3. The reservoir was then moved into the hot zone and where the entire 0.75 mL sample of Au/HCl solution B was added by dropper into the reservoir.
4. The reservoir was then resealed and shaken vigorous by hand for 4 minutes. During which, the reservoir was rotated throughout agitation to encourage even mixing.
5. The batch was stored in the reservoir until needed.

3.4.5 *Batch E Preparation*

Batch E was produced by adding 0.3118 g of radioactive gold powder to a standard resin. The powder was active by neutron generator.

1. Following manufacturer's directions, 100 mL of magenta pigment was added by syringe to 800 mL of Formlabs color base in its reservoir.
2. The reservoir was resealed and shaken vigorously by hand for 2 minutes and set aside.
3. The balance was tared to zero and a 1 mL plastic sample vial was weighed. The hinge on the vial was trimmed off for ease of encapsulation.
4. A wooden stirring rod was used to remove a small amount of gold powder its container and was poured into the weighed vial. The lid was resealed.
5. A second measurement was taken of the sample vial to find the wet weight.
6. The gold powder was double encapsulated it with PTFE tape and a secondary LDPE 7 mL vial.
7. This target was placed inside a custom arranged reaction chamber with the head of the nGen-800 neutron generator, see Figure 8. This reaction chamber was constructed to moderate and reflect the neutrons for better absorption in the target. It was constructed from concrete cider bricks, acrylic plastic panelling 0.5 cm in thickness, four large HDPE plastic blocks, and a lead brick for a pedestal.
8. The targets were irradiated for 12 hours at the 150 kV setting. The exact value of the neutron flux inside the chamber was not directly measured.
9. Immediately after irradiation the target was removed from chamber and counted on the HPGe for 10 minutes.

10. 420 mL of the magenta colored resin was measured out in a graduated cylinder and poured to a UV resistant screw top container. The mass of the resin was too great for the balance to read.
11. The powder was unsealed and upended into the UV resistant container with the magenta resin. A wooden stool was used to scrape the contents from the sides of the 1 mL vial.
12. The mechanical stirrer was used to mix the resin and powder at 1000 rpm for a minimum of 3 minutes.
13. The emptied sample vial was again measured on the balance to find the mass of the powder added to the resin.

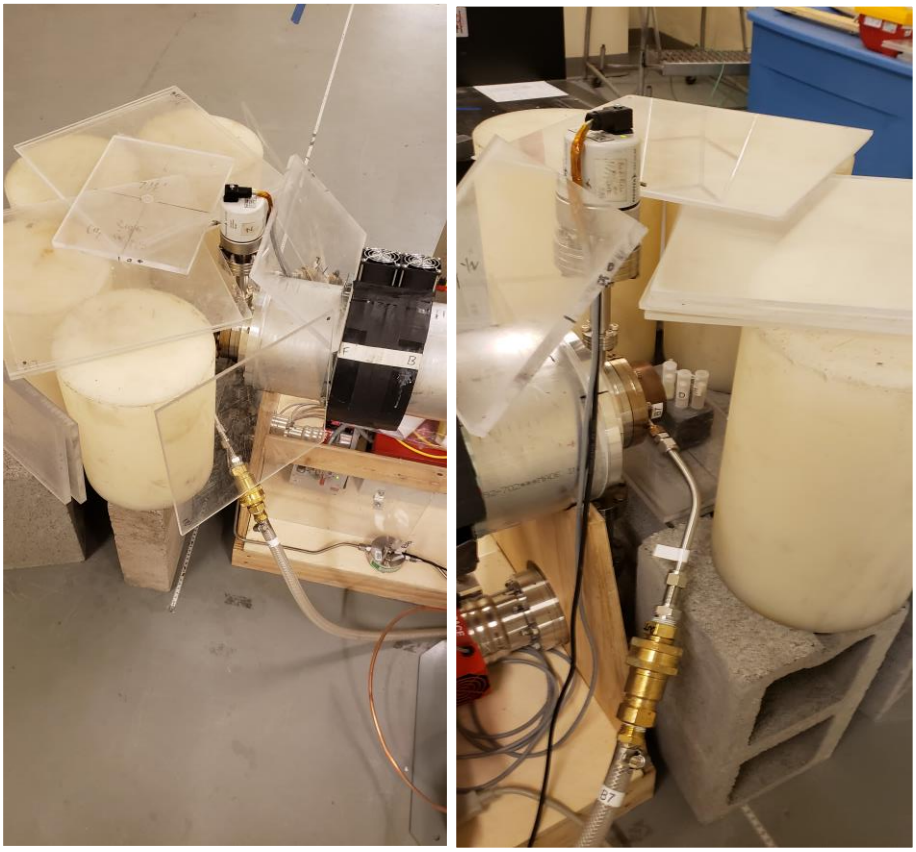

Figure 8 - nGen-800 neutron generator pictured inserted into acrylic reaction chamber (left). Plastic panel removed to reveal target samples perched atop a brick of lead inside the reaction chamber (right).

3.4.6 *Batch F Preparation*

1. 450 mL of magenta pigment from 3.4.5 Steps 1 and 2 was measured into a graduated cylinder beaker. This resin was then poured into an UV opaque screw top container.
2. From ^{198}Au/HCl solution F, 0.4 mL was aliquoted into the UV opaque container with the magenta resin.
3. The remaining 0.1 mL was aliquited into a similar preparation of elastic resin in a seperate UV opaque container with 450 mL of elastic resin.

4. Each mixture was mechanically stirred for a minimum of 3 minutes at 1000 rpm. The mixing rod and impeller was removed and cleaned with IPA and disposable shop towels in between batches to avoid contamination.

3.4.7 *Printing*

1. Stereolithography (STL) files for printing were either downloaded from open sources off the internet (MakerBot Industries LLC 2019) or drafted using Solidworks software.
2. The files were uploaded into a Formlabs program called Preform to modify the STL files in such a way to prepare them for printing.
3. After importing files, the shape of the build may be scaled or repositioned on the virtual platform. Figure 9 below is a screen capture of the Preform program after an STL file had been imported.

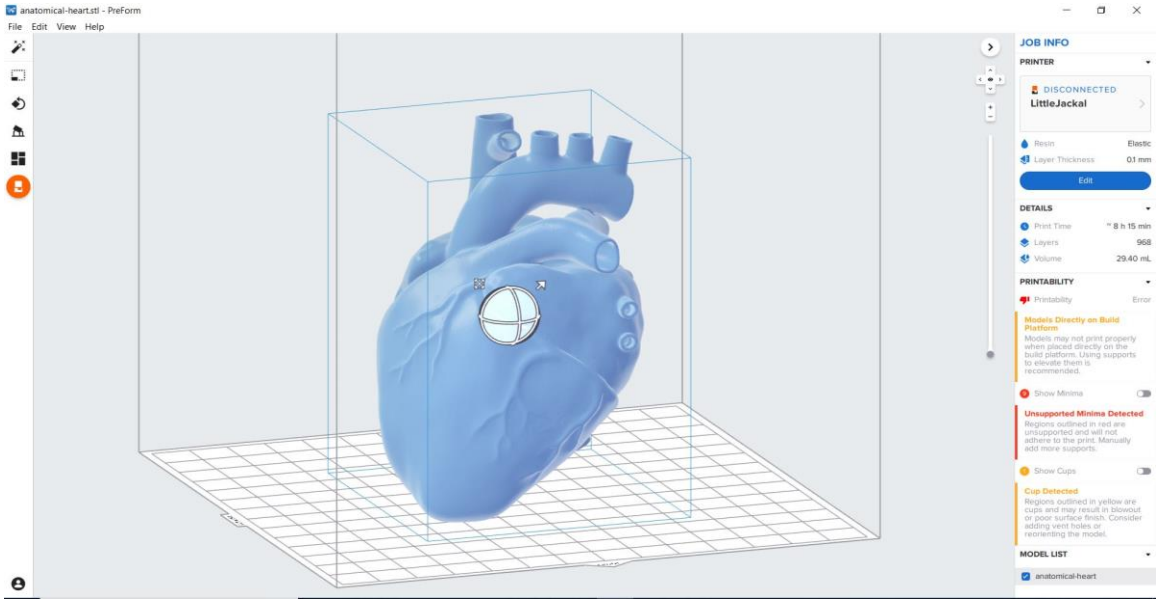

Figure 9 - Screenshot of Formlabs Preform software. Anatomical heart phantom has been imported into the Preform software with a virtual build platform.

4. The user selected the resin of choice so as to clue the printer to apply the appropriate forces or beam speeds.
5. Layer thickness was adjusted depending on the material selected and the desired resolution to alter the properties of build speed. Prints with a greater number of thin layers naturally have greater resolution but longer printing times. The program includes readouts such as anticipate printing times and the volume of resin required to complete the task. The user may add supports and scaffolding to prevent the build from collapsing during the print. A
6. The wizard feature was used to automatically orientate and apply scaffolding for the user. In Figure 10 below the anatomical heart from Figure 9 has been rotated and transposed to be closer to the edge of the build. The wizard adds small skids on the scaffolding to assist in the removal of the print from the build platform.

7. Once the wizard was complete, the job file was sent wireless to the Form 2 printer. Printing time ranged from 3 to 10 hours depending on the complexity and volume of the build.

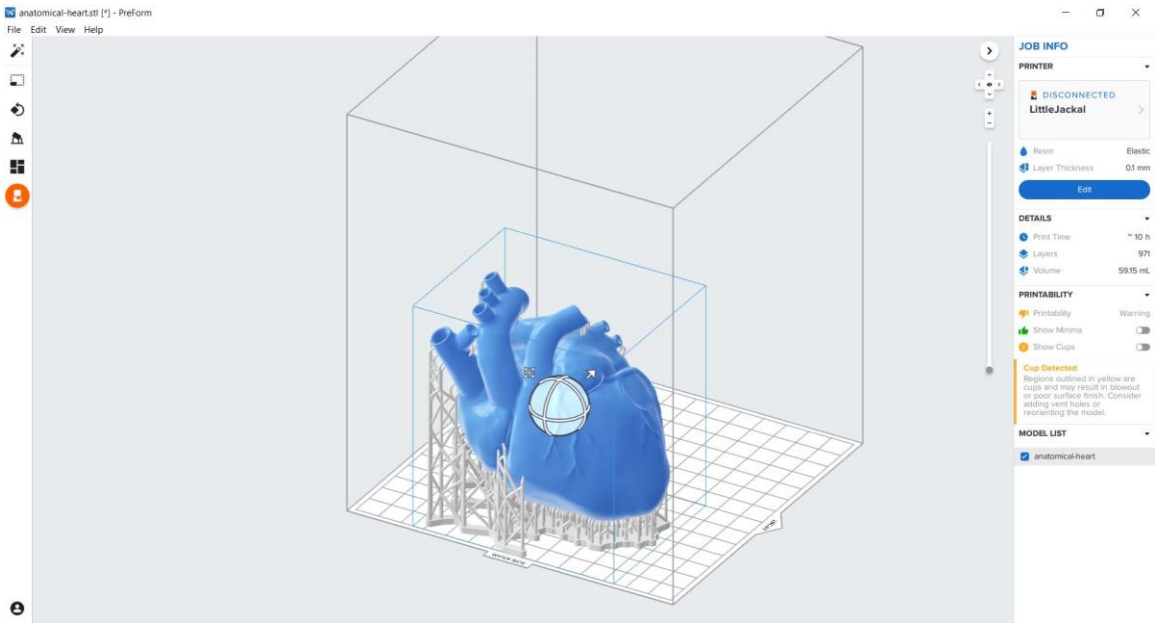

Figure 10 - Anatomical heart after the printing wizard has been used to auto-orientated the shape and automatically draft scaffolding.

3.4.8 *Post-printing*

1. The builds were allowed 15 minutes after printing had completed to drip dry back into the resin tray.
2. The build platform was removed from the Form 2 printer and placed over the Form Wash basket.
3. The builds were dislodged into the Form Rinse basket using spatulas and levered instruments.
4. The builds were washed in 90%+ isopropyl alcohol for 30 mins and allowed to air dry under a fume hood.

5. All scaffolding was removed from the build using shearing implements and tweezers.
6. The builds were placed into the Form Cure and treated at 60℃ for 60 minutes for standard resin or at 60℃ for 30 minutes for elastic resins.
7. After the builds had cured, they were swabbed with a cotton pad and sent to be tested on a background counter to check for contaminated residue. Builds not in use were kept in a dark, dry environment set aside for radioactive sources.

3.4.9 *Counting*

1. Standard procedures were followed to prepare the HPGe for counting. Assuming the detector started at room temperature, industrial grade liquid nitrogen was used to fill a dewar connected to the detector.
2. The apparatus was allowed to cool over the course of 12 hours prior to sample counting.
3. A bias voltage of 4300 V was applied through the Genie 2000 interface.
4. A plastic cap was inserted between the graphene screen and sample to provide a measure of protection to the window. This cap and an example of the radioactive prints may be seen in Figure 11 below.
5. Counting times were selected based on one of the following:
    a. An amount of time necessary to collect 10,000 counts based on the number of counts collected in a 10-minute interval, Batch A.
    b. One hour, Batch B and Batch E.
    c. An amount of time necessary to collect enough counts to reduce Gaussian statistical uncertainty below 2%, Batch F.

6. Once counting was complete, the spectrum was saved for later use and the next build was placed on the HPGe.
7. ROI were selected based on the area of the photopeak that resulted in a gaussian ratio closest to unity.

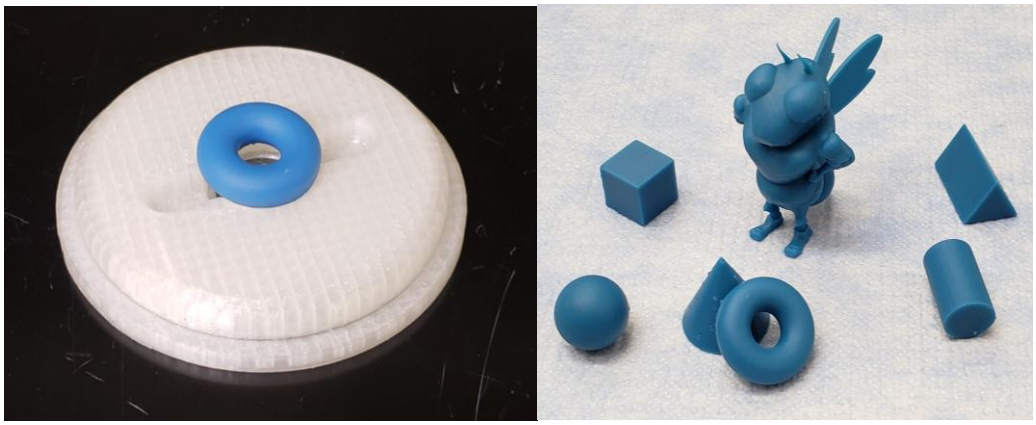

Figure 11 - Toroid build printed from Batch B set on top of plastic protection cap (Left). Display of the geometry builds and Georgia Tech mascot from Batch B (Right).

3.4.10 *Mass Measurements*

1. A cotton pad was placed on the stainless-steel balance dish to serve as a barrier to prevent contamination of the dish with possible residue from the prints. Separate cotton pads were not used as this would require a constant resetting of the tare weight and introduce additional error into the system. Therefore, a single cotton pad was used for all mass measurements to minimize uncertainty.
2. Each print was placed inside the balance. The doors on the balance were shut to avoid disturbance from air currents.
3. The balance was allowed to settle for 5 seconds and the reading from the display was recorded.

4. The side doors were opened and the print was removed and the process was repeated starting with Step 2.

CHAPTER 4. RESULTS

Chapter 4 will be broken down into four distinct sections. The first of which is energy efficiency calibrations. The second of will focus on homogeneity results on the activity and mass data. It will report the facts and figures of this data and make observations of its behavior and underlying patterns. Next the results of the geometric builds were analyzed for their efficiency. A comparison was made between the efficiencies of the various shapes and their deviations from their amorphous theoretical activities. Lastly, complications in the mixing and printing of the sources was reviewed.

Table 2 - Summary of batches printed.

	Batch A	Batch B	Batch E	Batch F
Active Matrix	0.918 g of 10 ppm Au/HCl	0.765 of 10 ppm Au/HCl	0.312 g of 1.5 μm dia. Au powder	0.408 g of 10 ppm Au/HCl
Activity	164 kBq	76.76 kBq	6.738 kBq	4.398 kBq
k	5.6 μg/Bq	9.97 μg/Bq	46.63 μg/Bq	9.28 μg/Bq
Mass Fraction, φ	0.211%	0.079%	0.068%	0.084%
Batch Vol.	400.90 mL	890.75 mL	420.02 mL	450.40 mL
Theo. Specific Activity	376.43 Bq/g	79.43 Bq/g	17.77 Bq/g	90.00 Bq/g
Reference Date	10/16/2018 8:30:00 AM	1/1/2019 8:30:00 AM	5/31/2019 1:00:00 PM	5/29/2019 8:30:00 AM

4.1 Efficiency Curve Calibration

Genie 2000 software was used to determine the number of counts under the relevant photopeaks. Table 1 and Equation 2 were used to calculate the efficiency of detection under these particular photopeaks. From them an interpolation was made with a polynomial fitting algorithm to produce the efficiency curve as shown in Figure 12 below. This calibration curve determined the HPGe detector had an efficiency of 5.85% at the 411.8 keV ^{198}Au energy peak.

The detector experienced its greatest theoretical efficiency of 25.4% at 64 keV and its lowest efficiency of 1.75% at 1167 keV. The differential change in efficiency across the energy spectrum in the vicinity of 411.8 keV was found to be $\pm 6.53 \frac{\%}{keV}$. Given the photopeak isn't prone to skewing the 5.85% efficiency may be used for energies close to 411.8. In contrast, efficiencies in the 140 keV region varied as much as $\pm 14.2 \frac{\%}{keV}$. The raw and calculated data for each calibration peak may be found in the appendix. The intrinsic efficiency was calculated from the photopeak efficiency. The solid angle was determined to be 0.7362 with a geometric efficiency of 0.0586. From Equation 6 and the intrinsic efficiency was determined to be within 4 decimals of unity. Nearly all the inefficiency was due to geometric losses. The intrinsic efficiency was likely lower indicated because of additional loss. These losses will be discussed later in 5.1.1.

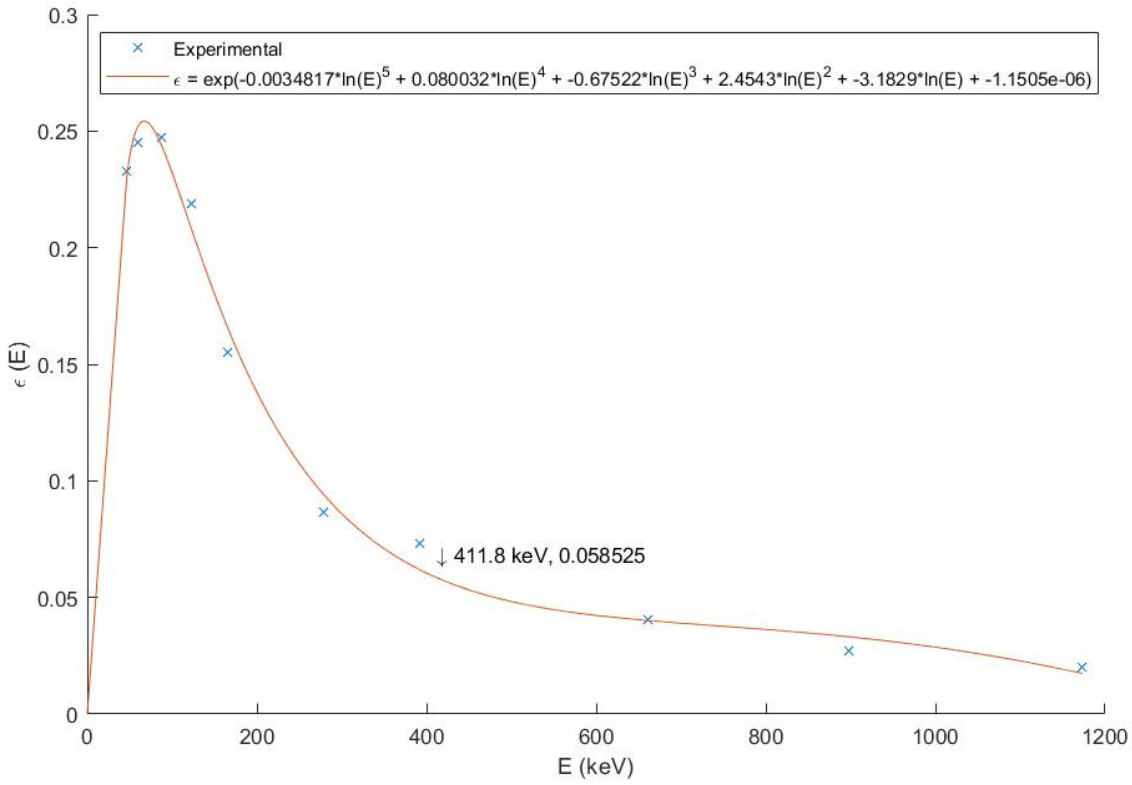

Figure 12- HPGe energy dependent efficiency curve based on a 5th degree polynomial fitting scheme of the Eckert and Zeigler multi-gamma standard counting results.

4.2 Homogeneity Results

Four different batches were examined for homogeneity. Equation 3 was used to calculate the activity of the sources at the initial survey time. In the following graphs, the mass of the test coupons was plotted on the abscissa and the initial activity was plotted on the ordinate. In a perfectly homogenous mixture, the activity in the coupons would be expected to increase linearly with mass. In Figure 13, the first results of doped resin were plotted.

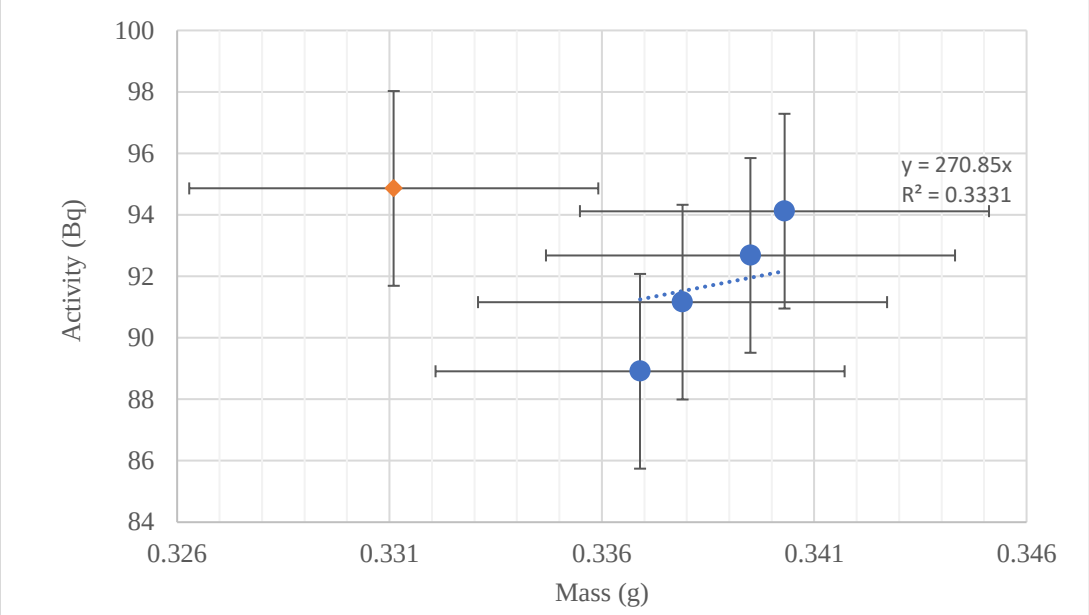

Figure 13 - Homogeneity test results from Batch A. The coupons in this batch were smaller than in others. ±3σ confidence intervals are included.

Most of the test coupons stayed between 0.336 g and 0.341 g. The data point in the far left of the graph indicated a significant outlier of the coupon from the grouping. This outlier was indicated with a different color diamond. Four of the data points indicated a small increase in activity with similar increases in mass. This was behavior expected from a uniform concentration. As the mass increases so too should the number of radioactive particulates occluded in the curing of the resin. A linear trendline was added to the four data points to determine a prospective relationship between activity and mass. A zero intercept was forced on the trendline for logical consistency. While the trendline stayed inside the confidence interval, the lower R^2 value indicated a tenuous correlation. Further discussion on this result may be found in 5.1.1. Despite the close values in masses, the activity of ^{198}Au measured in each coupon varied considerably. In fact, according to Table 3, the printing resolution of the Form 2 was high. The uncertainty of the masses in the coupons were typically lower than lower than 1% while the uncertainty in the activity of

the coupons was as high as 17.5 % for Batch B and as low as 3.6 % for Batch F. For this reason, the primary source of statistical uncertainty was less a contribution of mass variance in the printing process than of concentration variance.

Table 3 - Calculated specific activities and statistical data for printed batches. Specimens highlight and marked with a star denote specific activities outside the standard deviation.

	Batch A	Batch B	Batch E	Batch F
Avg (g)	0.3369	2.2708	2.27962	2.2932
STD (g)	0.0040	0.0051	0.0048	0.0074
σ_m/m (%)	±1.2	±0.22	±0.21	±0.32
Avg (Bq)	92.346	234.374	1.518	180.247
STD (Bq)	2.387	26.745	0.176	4.672
σ_A/A (%)	±2.6	±11.4	±11.6	±2.6
Avg (Bq/g)	274.072	103.212	0.666`	78.599
STD (Bq/g)	7.812	11.78	0.0772	2.053
σ_a/a%	±2.9	±11.4	±11.6	±2.6
M (%)	97.5	98.8	91.7	99.8
U_M (%)	±4.25	±0.096	±0.0094	±0.0037

The testing coupons from Batch A were smaller than ones from other batches. It was found that the small masses of the Batch A coupons took long counting periods, on the order of 6 to 12 hours, to accurately resolve. Following batches used test coupons with greater volumes and larger average masses. The greater volume resulted in test coupons that emitted sufficient photons for statistical accuracy within an hour of counting time. The standard deviations in the mass of the larger coupons were noticeably less than the smaller ones from Batch A while the uncertainty in their activities were greater.

Like Batch A, both Batch B and Batch F were radionuclides that originated from the TRIGA Mk II reactor in Austin, Tx. The Figure 14 below illustrates the efficacy with which

the two were mixed. Batch B, indicated by the blue circles, demonstrated unusual outliers in coupons 6B and 8B. Three of the coupons showed tight grouping around 2.268 g. The two other data points in Batch B seemed to indicate a strange relationship between a loss of activity with an increase mass. As there was no further evidence of such behaviour existing in other batches it was considered an artifact of the coupons. Likely, these deviations are a result of printing in regions of lowered concentrations. Batch F on the other hand showed tight grouping of activity between 170 Bq and 190 Bq but a broader variance in the mass, from 2.28 g to 2.95 g. It should also be noted here that while the exact form file was used in both prints, those of Batch F were slightly more massive on average than those in Batch B. This could have been a result of an increase in shrinkage between Batch B and Batch F or it could have been the result of a higher concentration of inert Au atoms in the matrix. The statistical standard error in activity was dramatically different between Batch B and Batch F. Batch F contained twice the number of test coupons as either of the other three batches.

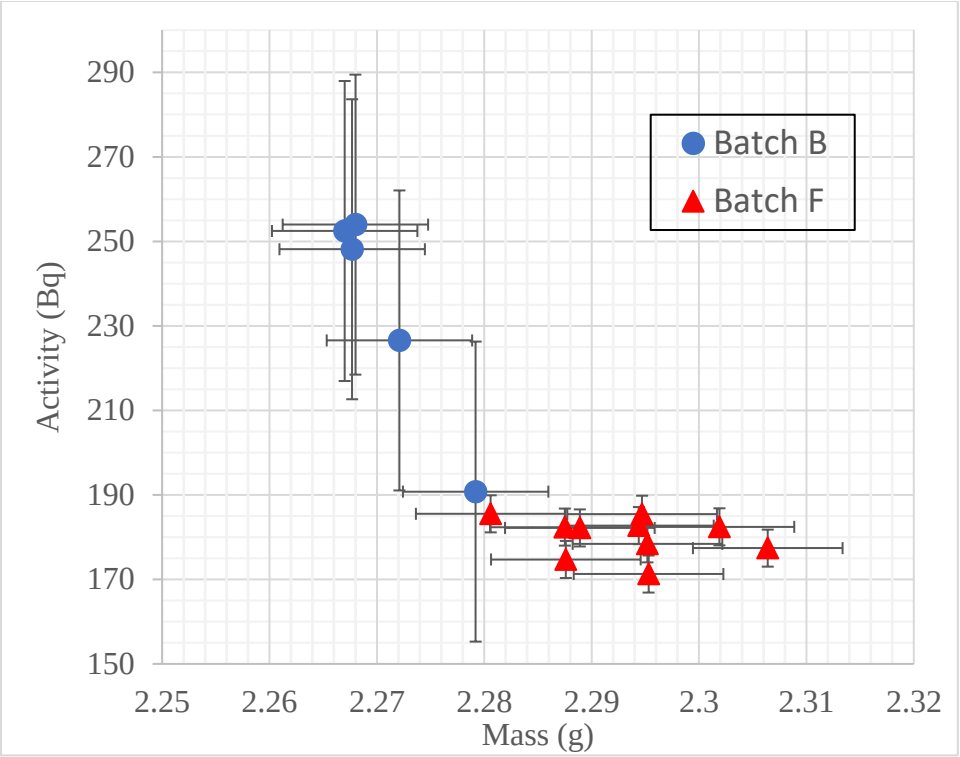

Figure 14- Calculated activity plotted against measured mass Batch B represented in blue circles and Batch F represented in red triangles. ±3σ confidence intervals are included for mass and activity.

The final batch examined was that of the gold nano powder activated by neutron generator. Like Batch A, the testing coupons from Batch E bared a similar linear relationship between the activity and mass as shown in Figure 15 below. Again the trendline was forced to a zero-mass *y*-intercept. The two outliers were excluded from the trendline and indicated as diamond. Of the all test coupons those in Batch E were the least active, much less so than those printed with sources traceable back to a fission reactor. Because the low activity these samples were difficult to identify as sources without the use of HPGe detector. Neither NaI(tl) nor CZT detectors were sensitive enough to register the activity at 411.8 keV.

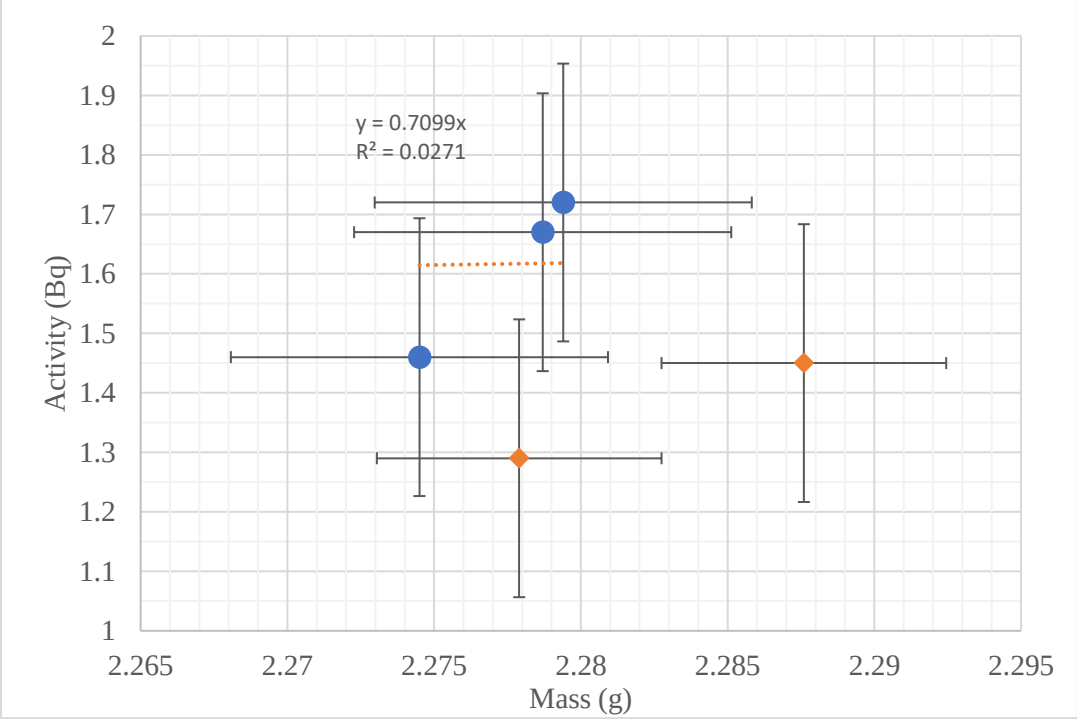

Figure 15- Batch E calculated activity plotted against measured mass. Outliers have been plotted separately as orange diamonds. ±3σ confidence intervals for mass and activity have been included.

4.3 Geometric Efficiency Results

The experimental specific activity from each batch was used to determine theoretical activities in each of the geometric builds in order to deduce their absolute and relative errors. A total of 18 builds were printed and counted using the same HPGe. Geometric shapes were only printed from Batch B, Batch E, and Batch F. Each build was weighed on the Mettler Toledo balance. Based on their mass and the experimental specific activity found in 4.2, a theoretical activity was produced based on the calibration source geometry and 4π collection of source quanta as shown in Table 4 below. These values have the same uncertainty as that which was calculated for the specific activity in Table 3.

Table 4 - Theoretical values for geometric build activity based on measured mass and experimental specific activities of corresponding batches.

	Batch B	Batch E	Batch F
Cone	583.30 Bq	3.734 Bq	440.45 Bq
Cube	596.79 Bq	3.830 Bq	451.44 Bq
Cylinder	578.15 Bq	3.699 Bq	436.51 Bq
Prism	603.00 Bq	4.431 Bq	462.1 Bq
Sphere	588.12 Bq	3.782 Bq	446.56 Bq
Torus	587.27 Bq	3.76 Bq	443.43 BQ

After counts were collected from the geometry builds their activity at t_o was calculated using Equation 3. Figure 16 shows a bar graph of efficiencies calculated for each geometric build using Equation 10. The geometric efficiency calculated from the calibration source was added to the graph as a reference. A majority agreement existed where two of the three batches showed similar trends in both magnitude. In the case of the cone and prism geometry there was strong majority agreement between Batch B and Batch F. Marginal majority agreement exists between Batch B and E of the sphere and Batch E and F of the cube. The torus and cylinder have poor majority agreement.

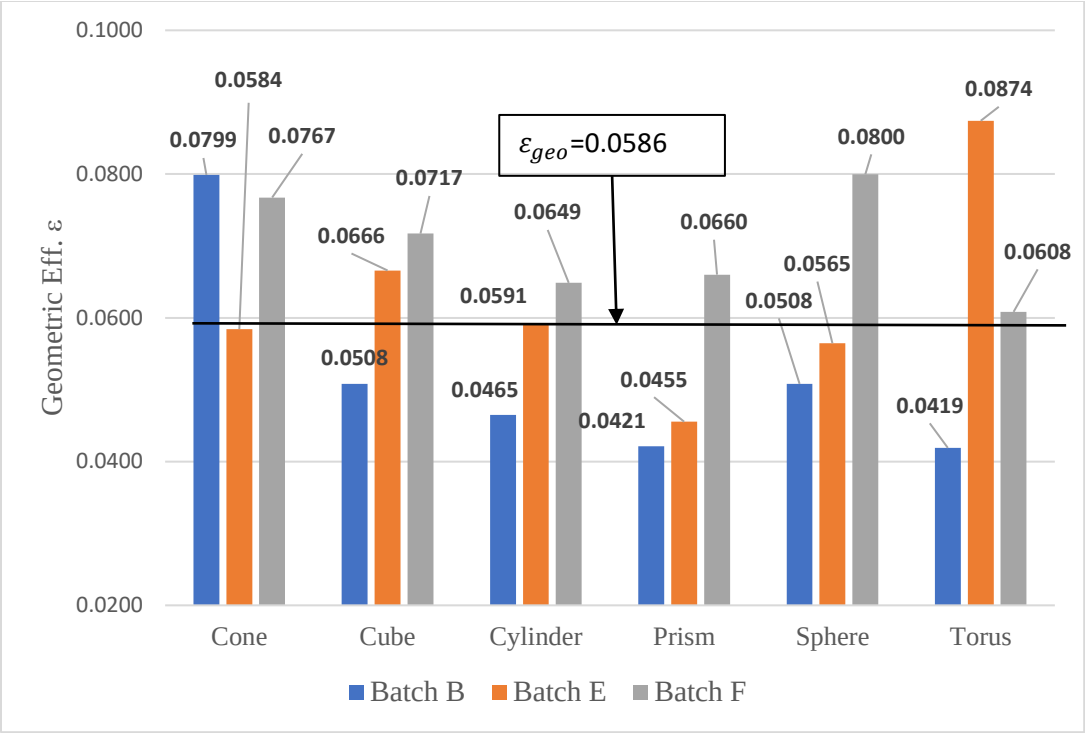

Figure 16 - Geometric efficiency calculated for each geometry built. Batch B (left columns) Batch E (center columns) Batch F (right columns).

Under each geometric heading, each batch was given a bar to represent the degree of deviation from the corresponding value in Table 4. The horizontal lines demark the respective uncertainty in each batch. Batch F demonstrated consistency in each geometric build category with a lower than projected activity. These deviations ranged from -32.02 % to -48.21 % and showed more consistency between each geometry than inside its own. In every geometry, Batch F found itself outside the limits explained by the homogeneity analysis. This was significant because of the batch's particularly high degree of homogeneity as calculated in its mixing number. The relative error values were calculated through Equation 11 and compared to the uncertainties in specific activity calculated in Table 3. The results are presented in Figure 17 below.

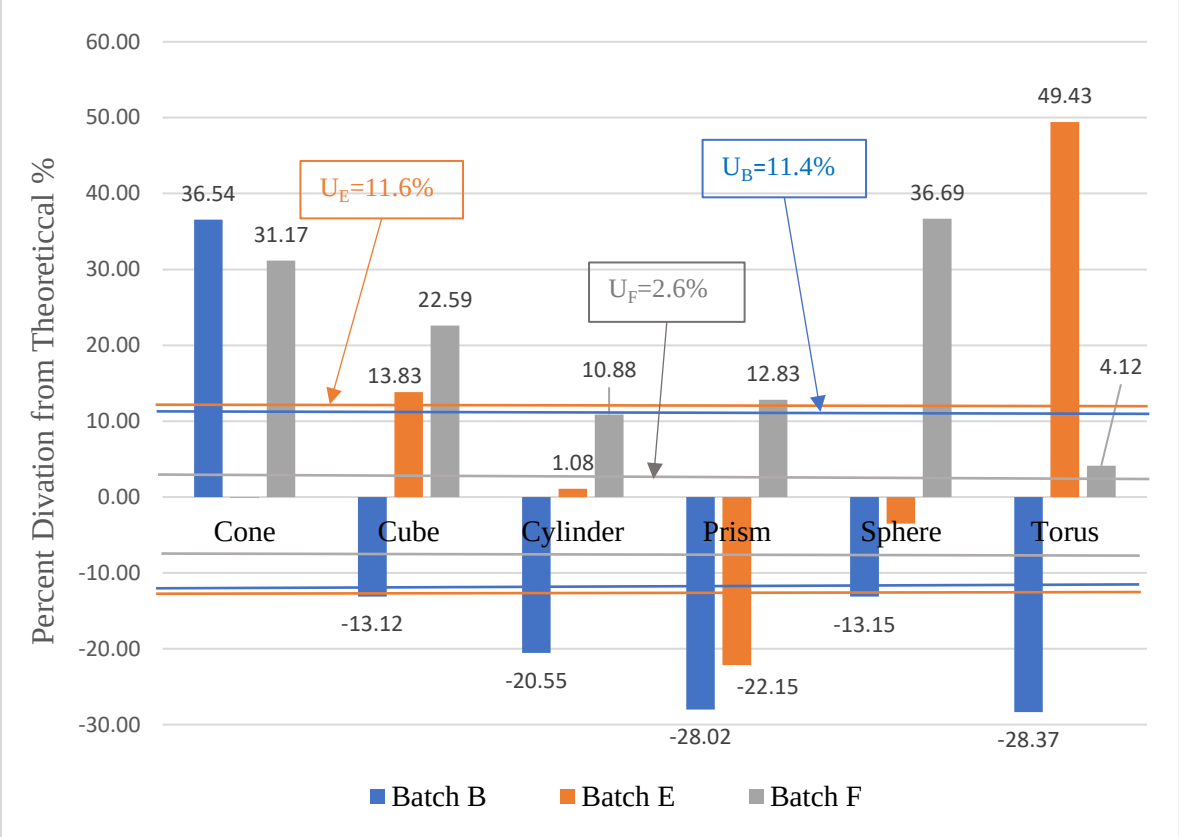

Figure 17– Relative error in each of the geometric builds and batches. Data labels were added to significant departures from theoretical values. Batch B (left columns) Batch E (center columns) Batch F (right columns).

Batch E and Batch B shared uncertainties as demarcated in Figure 17. However, their behavior in the geometric builds was quite different. Batch B saw strong deviations in the cone, cylinder, prism, and torus geometries. The cube and the sphere geometries were too close to U_B to associate the deviation with something other than inhomogeneity of concentration of radionuclides in the print. Likewise, in Batch E the experimental values in the cone, cylinder, cube, and sphere were either too close to, or well below, U_E and the influence from inhomogeneity overshadowed any deviations from geometry. As such these couldn't be contributed for or against characterization of the geometry.

In the cone, cube, and prism geometries two of the three batches showed coherence in the direction and magnitudes of deviation from the theoretical value. These coherences were not all from the same batch and could not reliably be used to discern a pattern. In the cylinder, cube, and torus, Batch B significantly departed from the other two batches in sign and magnitude.

The uncertainties in the activities of each batch were used to find experimentally based standards of deviation for each build. The deviation from the theoretical values were divided by the standard deviation for activity corresponding to batch.

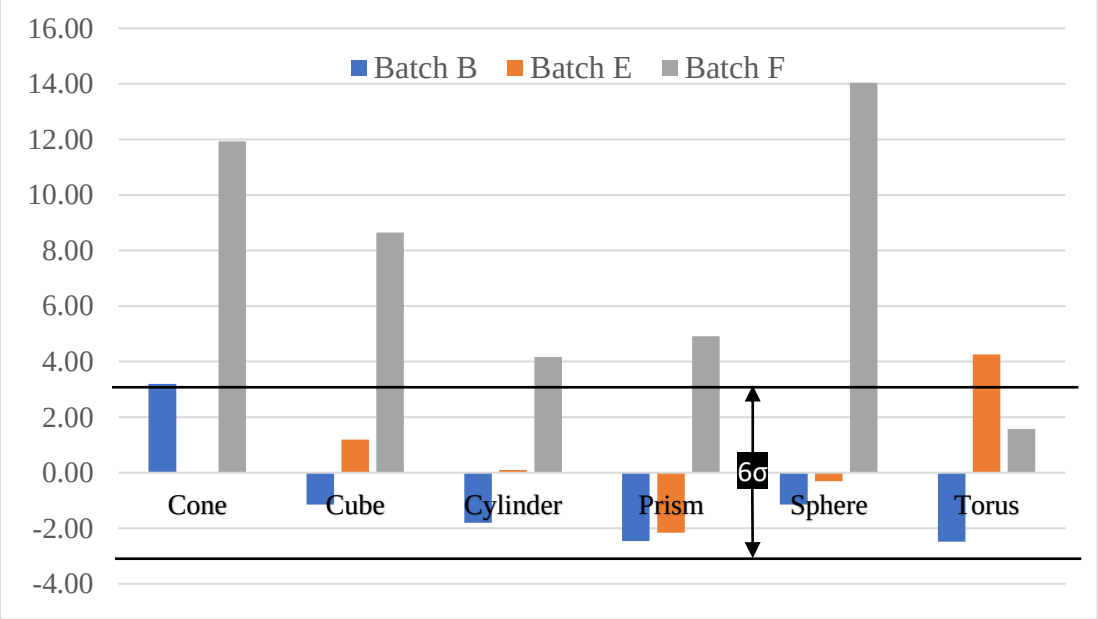

Figure 18 – Measured deviation from the theoretical uniform value in terms of experimental standard deviation as calculated from U_{act} in Table 3.

4.4 Complex Geometry

In order to verify the ability of this procedure to produce more complex shapes, an anatomical heart was printed using elastic resin. While a homogeneity test wasn't

performed on the combination of elastic resin and liquid Au/HCl matrix, the resin was assumed to be similar in nature to that of the standard. Elastic resin required a separate printing and curing scheme, one recommended by the manufacturer. The Form 2 printer produced a print with a measure mass of 55.75 g and a corrected activity of 103.9 Bq. The result was a ductile product with the ability to encapsulate radionuclides into a phantom structure with pliability. Figure 19 below provides a photograph of the radioactive phantom heart. The support structures printed inside the heart could not be removed without causing damage to the phantom.

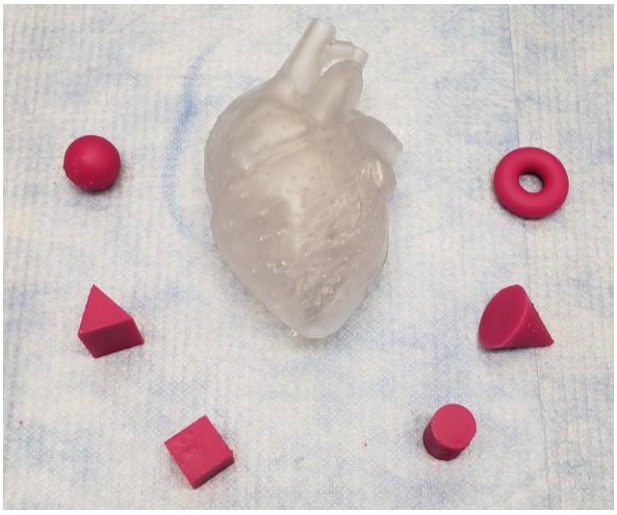

Figure 19 – Anatomical radioactive heart phantom accompanied with geometric builds from Batch F.

4.5 Complications

The resin used in the printing process responded to the doping with a variety of behaviours. Mixing HCl into the resin appears to have the effect of warping the elastic resin screen used to cushion the build against the curing window. The effect is not immediate and takes a matter of weeks to damage the screen to the point that distortions

occur in the printing process. The screen is required for proper printing as it prevents the builds from fusing directly to window. Further damage was inflicted to the tray itself, likely from the presence of HCl. The damage appeared to grow more visible with prolonged contact with the doped resin. IPA causes damage to the tray and screen much in the same way as HCl. No damage had accumulated on the tray used in Batch E. This is likely due to the inert nature of the gold powder.

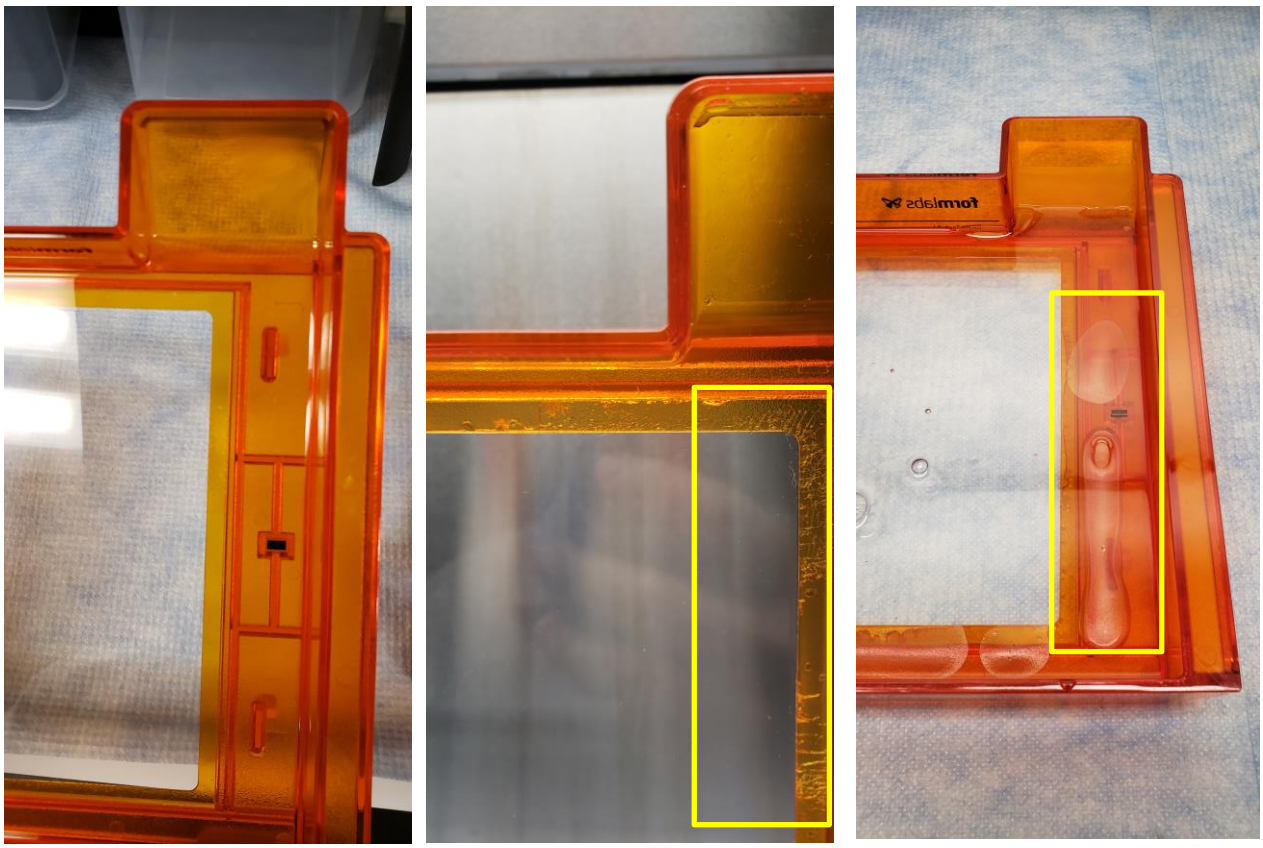

Figure 20 - Effect of HCl doped resins on tray integrity. Pristine tray shows little to no warpage or fretting (Left). Damage in the form of degradation after exposure to Batch A for 3 weeks (Center). Warpage in the elastic protection screen after 5 weeks exposure to elastic Batch F .

CHAPTER 5. DISCUSSION

5.1.1 *Error*

The first topic of error discussion will be error introduced into the homogeneity calculations. In order to sample the batches for homogeneity prints had to be made. The concentration of radionuclides were not evenly distributed through the materials, $\frac{dC}{dV} \neq 0$. In Batch A, the homogeneity test coupons were printed such that the final volume be 0.2 mL. This created a problem where the activity of the printed sources was so low that 6 hours or more was needed to collect enough photon interactions for statistical certainty. The choice was made instead to make the coupons larger to encapsulate more radionuclides. This however had the effect of reducing the resolution of the homogeneity. Using only an HPGe detector the spatial distribution of radionuclides in the test coupons could not be determined. The test coupons were treated as if they were uniformly distributed when in fact they were not. A better treatment of this method would include a resin with high activity that when printed in small volumes still produces enough disintegrations that they be measured quickly. This combination of finer volumes and greater number of prints would provide better accuracy of the homogeneity.

The intrinsic efficiency was calculated using dimensions measured from the Eckert and Zeigler multi-gamma standard. However, the source was itself sealed inside a cylindrical plastic vial which remained unbreached. Equation 7 uses normalized distances to calculate the solid angle. An isometric contraction of the dimensions would have little effect on the result, but any change in the relative dimensions would angle the solid angle.

A direct observation of the calibration source was not possible, but the tight tolerances of the vial left good reason to suggest the relative dimensions are similar.

The HPGe detector is not a perfect absorber of gamma photons and this fact leads to error in calculations of the efficiencies. The intrinsic efficiency for a 26 mm crystal is closer to that of 82% than unity (Strauss, et al. 1977). These include edge losses, non-uniformities in the structure of the germanium crystals, and Compton scattering losses. The typical germanium crystal bears a cylindrical shape from the manufacturing process. Radials drawn from a volume element in the sources that intersect with the crystal are considered part of the solid angle. However, not all radials have the same photon interaction probability. Edge losses result from the reduced path length through the crystal at the edges of the detector. The probability of interaction with the crystal decreases as a result. A series of calibration runs using a lead masks would need to be conducted in order to determine the extent of the losses. The second source of error comes from the non-uniformity. This non-uniformity results from dead layers in the crystal or from recombination and trapping in channels formed by the crystals manufacture which lead to errors close to the contacts (Strauss, et al. 1977). Without a thorough analysis of the crystal using beam line techniques the topographical flaws remain unknown. The third source of error mentioned involves Compton scattering redirecting the photon outside of the detection mass of the crystal. If the Compton scattering angle changes the trajectory in such a way that the photon is expelled from the crystal, particularly near the edges, the probability of interaction will be insufficient to absorb the photon in the detection mass. A treatment involving the products of the thickness dependant attenuation factors integrated over the solid angle would need to be conducted to account for these losses.

5.1.2 *Conclusions*

The doped resins were successfully printed using stereolithographic methods. The homogeneity of the batches varied considerably based on the methods used to mix them. Batch A and Batch F proved to be more uniform mixtures than that of Batch B or Batch E. While this work does validate the prospect of printing radioactive sources much more is required to refine the method. Gold dissolved in HCl makes for a simple additive but lacks sophisticated properties. The hydrochloric acid has an ill-effect on the plastics the resin trays were made. The rheology of HCl droplets in MMA were not fully explored either. The process of polymerization traps the matrix but to what degree is unknown. While curing, the resin undergoes a condition known as shrinkage (Jacobs 1992) where the density of the resin changes as the polymerization proceeds. As the density changes it isn't yet known how the matrix materials responds. The ratio of matrix mass that is occluded in the print versus the matrix mass that is excreted back into the liquid phase of the resin was not tested. Such an experiment would require high precision gamma spectrometry of liquid resins samples before and after printing a set of prints from the batch. A more in-depth homogeneity study needs to be made.

The linear trendlines for Batch A and E are considered tenuous due the large confidence intervals and small variation in the mass of the prints. To valid these trends a much larger sample size is required with graduated masses to provide unambiguous data (Cao, et al. 2019). A larger sample size will mean that a larger series of counts would need to be conducted on the HPGe. While ^{198}Au possesses helpful properties for safe usage, its half-life is too short to accommodate long counting times and large batch sizes. Likewise, a longer-lived radioisotope will be needed to examine the homogeneity of the batch over

long periods of time. Over time sedimentation and other disruptive forces might leech the droplets from the body of the resin or see smaller droplets fuse into larger droplets (Peters 1997). To observe such phenomena a longer-lived radioisotope must be used. An emulsifier or surfactant might be used to encourage and stabilize homogenization. The gold powder appeared to be a more stable option. The powder itself has little or no effect on the condition of the plastic containers and its particle distribution is much easier to calculate and compare with experimental results. The granules may still suffer from separation over time due to buoyancy effects (Berk 2013) but they are not subject to coalition as liquid droplets might.

The printing quality of the resin with tray heating and wiper motion was much better than that of resins printed in open mode. The reservoirs however make for difficult containers in which to mix the resin. The cavities and contours make for complex fluid flows. However, given the advantages of using the proprietary reservoir cartridge for printing it cannot be overlooked. Further trials should employ removing the resin from the reservoir, washing it out with IPA and drying it before refilling it with a prepared radioactive resin. This way the resin may be mixed completely, and the reservoir cartridge can still be used to print with the advanced features.

As a consequence of activating ^{197}Au in an HCl solution, the matrix in Batch A, B, and F had contained traces of ^{36}Cl and ^{35}S. Each of these primarily decay through a beta emission. The initial smear tests of newly cured parts suggest the activity of the residue were below minimum detectable amounts. More sensitive tests were ran by the Office of Radiation Safety at Georgia Tech which found detectable amounts of ^{35}S in the liquid resin. A more rigorous environmental study of these sources is due in future work.

Complex geometries were successfully printed, but evidence for use of geometric builds as an alternative to Monte Carlo computation remains inconclusive. Deviations in the activity of the geometric builds were large enough that inhomogeneity alone could not reasonably be counted as the cause. However, not enough builds were printed from each batch to provide consistent results on which to make sound determinations about the geometric efficiency characterizations of each shape. Highly homogeneous resins and large number of prints for each geometry are needed for definitive results. The phantom radioactive anatomical heart and Georgia Tech mascot were perhaps the most impressive builds from the lot. These two showed that complex prints can be made to provide useful tools for gamma cameras and spectrographs.

APPENDIX A

A.1 Scripts

Table 5 - Activity calculator. Decay constant computed in units of hours. End of irradiation was hard coded for each batch.

```
counts = input('Counts?'); %raw counts
gm = 0.95; %411.8 keV intensity
eff = 0.0585; %0.0585 detector efficiency
lam = 0.01072; %decay constant for Au198 in 1/hours
td1 = ['29-MAY-2019 13:00']; % end of irradiation period
td1 = datevec(td1);
td2 = input('Count start: dd-mmm-yyyy HH:MM:SS','s');
%start time of counting
td2 = datevec(td2);
tc = input('Count Time in hours'); % number f hours in
decimal form
td = etime(td2,td1)/3600; %etime outputs elapsed time in
seconds, converted to hours
A = counts/3600;
B = lam/(gm*eff);
C = (1-exp(-lam*tc))*(exp(-lam*td));
Act = (A*B)/C;
Actprt = strcat(num2str(Act),' Bq')
```

Table 6 - Efficiency calculation curves. Individual energies and efficiencies are fitted using a polynomial fitting of log energies.

```
x = [46.6 59.6 88.1 122.1 165.9 279.2 391.7 661.7 898
1173.1];
y = [0.233 0.245 0.247 0.219 0.155 0.0864 0.0731
0.0407 0.0269 0.0203];
xx = 46.6:0.1:1173.1;
p = polyfit([0 log(x)],[0 y],5);
yy = polyval(p,[0 log(xx)]);
Au = polyval(p, log(411.8))
k = polyder(p);
```

```
zz = polyval(k,log(411.8))
zz = polyval(k,log(140))
Auu = num2str(Au);
t1 = [num2str(p(1)) '*ln(E)^5'];
t2 = [num2str(p(2)) '*ln(E)^4'];
t3 = [num2str(p(3)) '*ln(E)^3'];
t4 = [num2str(p(4)) '*ln(E)^2'];
t5 = [num2str(p(5)) '*ln(E)'];
t6 = [num2str(p(6))];
eq = ['\epsilon = ' 'exp(' t1 ' + ' t2 ' + ' t3 ' + '
t4 ' + ' t5 ' + ' t6 ')'];

hold on
plot(x, y, 'x',[0 xx],yy)
axis([0 1200 0 0.3])
xlabel('E (keV)')
ylabel('\epsilon (E)')
text(411.8,(Au+0.01), ['\downarrow 411.8 keV, ' Auu]
)
legend('Experimental',eq)
```

A.2 Data

Table 7 - Multi-gamma standard efficiency curve data points. Initial activity was given by Ecker and Ziegler certification data. Certification date was Jan 1st 2018 12:00. Counting date was Oct 18th 2018. Counting time was 3600 seconds.

Isotope	Half-life	Init Act	λ	Calc Act	Exp Act	ϵ
Pb210	8.11E+03	1.45E+04	3.56E-06	1.41E+04	3295.85	2.330E-01
Am241	1.58E+05	1.16E+03	1.83E-07	1.16E+03	284.41	2.451E-01
Cd109	4.61E+02	1.61E+04	6.26E-05	1.04E+04	2565.73	2.467E-01
Co57	2.72E+02	3.65E+02	1.06E-04	1.74E+02	38.02	2.186E-01
Ce139	1.38E+02	5.50E+02	2.10E-04	1.27E+02	19.7	1.552E-01
Hg203	4.66E+01	1.19E+03	6.20E-04	1.56E+01	1.348	8.636E-02
Sn113	1.15E+02	9.41E+02	2.51E-04	1.63E+02	11.927	7.315E-02
Cs137	1.10E+04	4.61E+02	2.63E-06	4.53E+02	18.418	4.067E-02
Y88	1.07E+02	1.58E+03	2.71E-04	2.38E+02	6.397	2.691E-02
Co60	1.93E+03	7.22E+02	1.50E-05	6.50E+02	13.184	2.028E-02

Batch A	10/16/2018 8:30	164 kBq					
Coupon	Mass	Area	Err ±%	Ratio	FWHM (keV)	tc (secs)	Date
1A	0.3395	10592	0.98	1.052	2.011	25200	10/25/2018 22:47
2A	0.3379	10073	1	1.049	2.001	21600	10/25/2018 12:02
3A	0.3369	8797	1.08	1.021	1.995	25200	10/26/2018 12:14
4A	0.3403	24027	0.65	1.041	1.992	43200	10/24/2018 19:38
5A	0.3301	10871	0.97	1.038	2.003	32400	10/26/2018 20:59

Batch B	1/8/2019 8:30	76.76 kBq					
Coupon	Mass (g)	Area	Err ±%	Ratio	FWHM (keV)	tc (secs)	Date
6B	2.2721	6985	1.21	1.022	1.388	3600	1/15/2019 14:27
7B	2.267	7684	1.15	1.034	1.388	3600	1/15/2019 15:39
8B	2.2792	5738	1.33	1.024	1.388	3600	1/15/2019 16:46
9B	2.2677	7353	1.17	1.037	1.388	3600	1/15/2019 18:09
10B	2.268	7440	1.17	1.023	1.388	3600	1/15/2019 19:13
ConeB	5.6515	53803	0.57	1.022	1.388	3600	1/12/2019 13:17
CylinB	5.6016	29211	0.59	1.012	1.388	3600	1/12/2019 18:55
PrismB	5.8424	28578	0.6	1.023	1.388	3600	1/12/2019 15:41
SphereB	5.6982	34011	0.55	1.018	1.388	3600	1/12/2019 14:38
CubeB	5.7822	35028	0.54	1.022	1.388	3600	1/12/2019 13:17
TorusB	5.6899	27055	0.61	1.013	1.388	3600	1/12/2019 17:52

Batch E	5/31/2019 13:00	6.735 kBq					
Coupon	Mass (g)	Area	Err ±%	Ratio	FWHM (keV)	tc (secs)	Date
1E	2.2794	93	11.75	0.97	2.169	3600	6/5/2019 14:42
2E	2.2745	78	12.95	1.037	1.88	3600	6/5/2019 15:44
3E	2.2779	68	13.94	1.034	1.857	3600	6/5/2019 16:46
4E	2.2787	87	11.53	0.785	1.85	3600	6/5/2019 18:03
5E	2.2876	76	12.96	0.996	1.814	3600	6/5/2019 17:33
CubeE	5.7522	132	9.2	0.96	1.782	3600	6/7/2019 20:37
TorusE	5.6481	176	7.9	0.853	1.85	3600	6/7/2019 17:25
CylinE	5.5562	157	8.37	0.983	1.328	3600	6/6/2019 14:14
PrismE	5.8726	114	10.04	1.079	1.786	3600	6/7/2019 12:27
SphereE	5.68	150	8.62	1.058	1.715	3600	6/6/2019 16:06
ConeE	5.6074	149	8.7	1.045	1.756	3600	6/6/2019 18:42

Batch F	5/29/2019 8:30	43.98 kBq					
Coupon	Mass (g)	Area	Err ±%	Ratio	FWHM (keV)	tc (secs)	Date
1F	2.3019	5995	1.3	0.991	1.812	1800	6/2/2019 20:36
2F	2.2952	5829	1.31	0.999	1.825	1800	6/2/2019 21:08
3F	2.2953	5550	1.35	0.961	1.839	1800	6/2/2019 21:54
4F	2.3064	5665	1.33	1.001	1.82	1800	6/2/2019 23:16
5F	2.2944	5803	1.32	0.993	1.82	1800	6/2/2019 23:47
6F	2.2889	4826	1.44	0.947	1.832	1800	6/3/2019 16:42
7F	2.2806	4883	1.44	0.973	1.824	1800	6/3/2019 17:18
8F	2.2876	4566	1.49	0.966	1.832	1800	6/3/2019 17:58
9F	2.2947	4818	1.44	1.021	1.826	1800	6/3/2019 18:30
10F	2.2875	4707	0.46	0.984	0.984	1800	6/3/2019 19:08
TorusF	5.6417	4199	1.55	1.027	1.83	3600	6/10/2019 12:50
ConeF	5.6038	5196	1.39	0.955	1.84	3600	6/10/2019 13:53
CylinF	5.5536	4060	1.58	0.963	1.841	3600	6/10/2019 20:23
SphereF	5.6815	5428	1.36	0.99	1.842	3600	6/10/2019 14:56
CubeF	5.7436	4702	1.47	0.971	1.831	3600	6/10/2019 19:11
PrismF	5.8792	4510	1.5	0.964	1.826	3600	6/10/2019 17:31
heart	55.7505	561	4.29	1.03	1.836	3600	6/12/2019 13:33

A.3 Sample Calculations

Activity calculation for coupon 6B from Batch B

$$A_{so} = \frac{\lambda N}{\varepsilon I e^{-\lambda t}(1 - e^{-\lambda t_c})}$$

$$= \frac{\left(0.01072\ \frac{1}{hr}\right)(6985\ counts)}{(0.0585)(0.95)\left(3600\ \frac{sec}{hrs}\right)e^{\left(\frac{-0.01072}{hr} * 173.95\ hr\right)}\left(1 - e^{-\left(\frac{-0.01072}{hr} * 1\ hr\right)}\right)}$$

$$= \frac{74.88\ \frac{disintegration}{hr}}{\left(200.07\frac{sec}{hr}\right)e^{(-1.867)}(1 - e^{(-0.01072)})} = \frac{0.3742\ Bq}{(0.15458)(0.01066)} = 227.087\ Bq$$

Statistical standard deviation of Batch A

$$\left(\frac{\sigma_{\bar{a}}}{\bar{a}}\right)^2 = \left(\frac{\sigma_{\bar{A}}}{\bar{A}}\right)^2 + \left(\frac{\sigma_{\bar{m}}}{\bar{m}}\right)^2$$

$$\left(\frac{\sigma_{\bar{a}}}{\bar{a}}\right)^2 = (3.6\ \%)^2 + (1.2\ \%)^2$$

$$\left(\frac{\sigma_{\bar{a}}}{\bar{a}}\right)^2 = 14.4$$

$$\frac{\sigma_{\bar{a}}}{\bar{a}} = \pm 3.795\ \% = \pm 3.8\%$$

A.4 Tabulated Uncertain Calculations and Values

Uncertainty	Source	$\sigma^2 =$	Batch A	Batch B	Batch E	Batch F
Matrix Vol.	Wheaton Socorex Pipette	$(V_x * \pm 0.5\%)^2$	2.025×10^{-5} $(mL)^2$	1.40×10^{-5} $(mL)^2$	N/A	4.0×10^{-6} $(mL)^2$
Matric Den.	Inorganic Ventures	$\left(0.055\ \frac{\mu g}{mL}\right)^2$	2.75×10^{-2} $(\mu g/mL)^2$	2.7×10^{-2} $(\mu g/mL)^2$	N/A	2.7×10^{-2} $(\mu g/mL)^2$
Au/HCl Mass	Error Prop	$m_x^2\left[\frac{\sigma_{Vx}^2}{V_x^2}+\frac{\sigma_{\rho x}^2}{\rho_x^2}\right]$	2.23×10^{-2} g^2	1.54×10^{-2} g^2	N/A	4.40×10^{-3} g^2
Count Area	Canberra :HPGe	$(N * \%err)^2$	13091.6	7150.9	101.8	5812.6
Peak Energy	Canberra :HPGe	$\left(\frac{FWHM}{2.35}\right)^2$	3.62 $(keV)^2$	1.74 $(keV)^2$	3.33 $(keV)^2$	3.01 $(keV)^2$
Sample Mass	Mettler Toledo: Balance	$\left(\frac{0.0001\ g}{2}\right)^2$	2.5×10^{-9} g^2			
Resin Vol.	Beaker	$\left(\frac{50\ mL}{2}\right)^2$	625 $(mL)^2$			
Resin Density	Formlabs	$\left(\frac{1.09-1.08\ g/cm^3}{2}\right)^2$	2.5×10^{-7} $(g/cm)^{23}$			
Powder Mass	Error Prop	$3\sigma_{ms}^2$	N/A	N/A	7.5×10^{-9} g^2	N/A
Resin Mass	Error Prop	$m_r^2\left[\frac{\sigma_{Vr}^2}{V_r^2}+\frac{\sigma_{\rho r}^2}{\rho_r^2}\right]$	740 g^2	756 g^2	740 g^2	741 g^2
Peak Efficiency	Error Prop	$\left(\frac{0.0655}{keV}\right)^2\sigma_E^2$	0.0155	0.00746	0.0143	0.0129
Activity (A_x)	Error Prop	$A^2\left[\frac{\sigma_N^2}{N^2}+\frac{\sigma_\varepsilon^2}{\varepsilon^2}\right]$	N/A	N/A	1.9×10^{8} Bq^2	N/A
Activity (A_s)	Error Prop	$A^2\left[\frac{\sigma_N^2}{N^2}+\frac{\sigma_\varepsilon^2}{\varepsilon^2}\right]$	48306 Bq^2	151246 Bq^2	12.21 Bq^2	136162 Bq^2
k Au/HCl	Error Prop	$k^2\left[\frac{\sigma_{Vx}^2}{V_x^2}+\frac{\sigma_{\rho x}^2}{\rho_x^2}+\frac{\sigma_{Ax}^2}{A_x^2}\right]$	8.29×10^{-13} $(g/Bq)^2$	2.63×10^{-12} $(g/Bq)^2$	N/A	2.28×10^{-12} $(g/Bq)^2$
k powder	Error Prop	$k^2\left[\frac{\sigma_{mx}^2}{m_x^2}+\frac{\sigma_{Ax}^2}{A_x^2}\right]$	N/A	N/A	9.11×10^{-9} $(g/Bq)^2$	N/A
Geometric Efficiency	Error Prop	$\varepsilon_g^2\left[\frac{\sigma_N^2}{N^2}+\frac{\sigma_\varepsilon^2}{\varepsilon^2}\right]$	N/A	N/A	N/A	N/A
Mass Frac.	Error Prop	$(S_o^2)^2\left[\frac{\sigma_{mx}^2}{m_x^2}+\frac{\sigma_{mr}^2}{m_r^2}\right]$	1.74×10^{-4}	2.5×10^{-5}	1.81×10^{-5}	2.77×10^{-5}
Sample Mass Frac.	Error Prop	$\varphi_s^2\left[\frac{\sigma_k^2}{k^2}+\frac{\sigma_{As}^2}{A_s^2}+\frac{\sigma_{ms}^2}{m_s^2}\right]$	0.141	0.0329	1.02×10^{-4}	0.0224
S_o^2Variance	Error Prop	$(1-2\varphi)^2\sigma_\varphi^2$	5.82×10^{-5}	1.77×10^{-5}	1.35×10^{-5}	1.91×10^{-5}
S^2 Variance	Error Prop	$\frac{4}{(N-1)^2}\left(\sum_1^N(\varphi_s-\varphi)_i\right)^2(\sigma_{\varphi s}^2+\sigma_\varphi^2)$	2.93×10^{-3}	1.21×10^{-4}	3.17×10^{-6}	1.24×10^{-4}
Mixing Number	Error Prop	$\frac{4S^2}{S_o^4}(\sigma_S^2+\sigma_{So}^2)$	1.8×10^{-3}	9.15×10^{-5}	8.74×10^{-5}	1.37×10^{-5}

APPENDIX B

B.1 Standard resin technical data

Material Properties Data

	METRIC[1]		IMPERIAL[1]		METHOD
	Green[2]	Post-Cured[3]	Green[2]	Post-Cured[3]	
Tensile Properties					
Ultimate Tensile Strength	38 MPa	65 MPa	5510 psi	9380 psi	ASTM D 638-10
Tensile Modulus	1.6 GPa	2.8 GPa	234 ksi	402 ksi	ASTM D 638-10
Elongation at Failure	12 %	6.2 %	12 %	6.2 %	ASTM D 638-10
Flexural Properties					
Flexural Modulus	1.25 GPa	2.2 GPa	181 ksi	320 ksi	ASTM C 790-10
Impactl Properties					
Notched IZOD	16 J/m	25 J/m	0.3 ft-lbf/in	0.46 ft-lbf/in	ASTM D 256-10
Temperature Properties					
Heat Deflection Temp. @ 264 psi	42.7 °C	58.4 °C	108.9 °F	137.1 °F	ASTM D 648-07
Heat Deflection Temp. @ 66 psi	49.7 °C	73.1 °C	121.5 °F	163.6 °F	ASTM D 648-07

[1] Material properties can vary with part geometry, print orientation, print settings, and temperature.

[2] Data was obtained from green parts, printed using Form 2, 100 µm, Clear settings, without additional treatments.

[3] Data was obtained from parts printed using Form 2, 100 µm, Clear settings and post-cured with 1.25 mW/cm^2 of 405 nm LED light for 60 minutes at 60 °C.

Solvent Compatibility

Percent weight gain over 24 hours for a printed and post-cured 1 x 1 x 1 cm cube immersed in respective solvent:

Solvent	24 hr weight gain (%)	Solvent	24 hr weight gain (%)
Acetic Acid, 5 %	< 1	Hydrogen Peroxide (3 %)	< 1
Acetone	sample cracked	Isooctane	< 1
Isopropyl Alcohol	< 1	Mineral Oil, light	< 1
Bleach, ~5 % NaOCl	< 1	Mineral Oil, heavy	< 1
Butyl Acetate	< 1	Salt Water (3.5 % NaCl)	< 1
Diesel	< 1	Sodium hydroxide (0.025 %, pH = 10)	< 1
Diethyl glycol monomethyl ether	1.7	Water	< 1
Hydrolic Oil	< 1	Xylene	< 1
Skydrol 5	1	Strong Acid (HCl Conc)	distorted

9. Physical & Chemical Properties

Appearance: Liquid, white color
Odor: Light/Characteristic/Acrylate

	Value	Unit	Method
Specific Gravity	1.08 – 1.09	g/cm^3	
Boiling Point	> 100	°C	
Flash Point	> 100	°C	
Ignition Temperature	no data		
Lower Explosion Limit	no data		
Upper Explosion Limit	no data		
Viscosity	850 – 900	cps	@ 25 °C (77 °F)

Vapour Pressure: Not established
Solubility in Water: Only very slightly soluble
Solubility in Organic Solvents: Soluble in organic solvents
Volatile Characteristics: Negligible
Electrostatic Discharge: Safe
Electric Conductivity: Dielectric

B.2 Elastic resin technical data

Material Properties Data

	METRIC[1]		IMPERIAL[1]		METHOD
	Green	Post-Cured[2]	Green	Post-Cured[2]	
Ultimate tensile strength [3]	1.61 MPa	3.23 MPa	234 psi	468 psi	ASTM D 412-06 (A)
Stress at 50% elongation	.92 MPa	.94 MPa	133 psi	136 psi	ASTM D 412-06 (A)
Stress at 100% elongation	1.54 MPa	1.59 MPa	223 psi	231 psi	ASTM D 412-06 (A)
Elongation at Failure [3]	100%	160%	100%	160%	ASTM D 412-06 (A)
Compression set at 23C for 22 hrs	2%	2%	2%	2%	ASTM D 395-03 (B)
Compression set at 70C for 22 hrs	3%	9%	3%	9%	ASTM D 395-03 (B)
Tear strength [4]	8.9 kN/m	19.1 kN/m	51 lbf/in	109 lbf/in	ASTM D 624-00
Shore hardness	40A	50A	40A	50A	ASTM 2240

[1] Material properties can vary with part geometry, print orientation, print settings and temperature.

[2] Data was obtained from parts printed using Form 2, 100 µm, Elastic settings, washed in Form Wash for 20 minutes and postcured with Form Cure at 60C for 20 minutes.

[3] Tensile testing was performed after 3+ hours at 23 °C, using a Die C dumbbell and 20 in/min cross head speed.

[4] Tear testing was performed after 3+ hours at 23 °C, using a Die C tear specimen and a 20 in/min cross head speed

Solvent Compatibility

Percent weight gain over 24 hours for a printed and post-cured 1 x 1 x 1 cm cube immersed in respective solvent:

Mechanical Properties	24 hr size gain (%)	24 hr weight gain (%)	Mechanical Properties	24 hr size gain (%)	24 hr weight gain (%)
Acetic Acid, 5 %	<1	2.8	Hydrogen Peroxide (3 %)	<1	2.2
Acetone	19.3	37.3	Isooctane	<1	3.5
Isopropyl Alcohol	13.3	25.6	Mineral Oil, light	<1	<1
Bleach, ~5 % NaOCl	<1	2	Mineral Oil, heavy	<1	<1
Butyl Acetate	18.2	39.6	Salt Water (3.5 % NaCl)	<1	1.7
Diesel	1.2	4.2	Sodium hydroxide (0.025 %, pH = 10)	<1	2
Diethyl glycol monomethyl ether	12	28.6	Water	<1	2.3
Hydrolic Oil	<1	2.1	Xylene	20.4	46.6
Skydrol 5	9.9	21.7	Strong Acid (HCl Conc)	14.2	39.4

9. Physical & Chemical Properties

Appearance: Liquid, light violet color
Odor: Light/Characteristic/Acrylate

	Value	Unit	Method
Specific Gravity:	1.02	g/cm^3	
Boiling Point:	> 100	°C	
Flash Point:	> 93.5	°C	
Ignition Temperature:	n.d.		
Lower Explosion Limit:	n.d.		
Upper Explosion Limit:	n.d.		
Viscosity:	~1,650	cps	@ 40°C (104°F)

Vapour Pressure: Not established
Solubility in Water: Only very slightly soluble
Solubility in Organic Solvents: Soluble in organic solvents
Volatile Characteristics: Negligible
Electrostatic Discharge: Safe
Electric Conductivity: Dielectric

B.3 Eckert and Ziegler Certification

SRS Number: 108401A

Comments:
Approximate volume: 0.19 mL

Expiration Date: 05-February-2019

This source was wipe tested in its inactive areas with leak test results < 185 Bq (5 nCi) of removable activity per ISO 9978:1992.

Source Prepared by: _____
Z. Dimitrova, Radiochemist

QC Approved by: _____ Date: 31-JAN-18
J. Lahr, Spectroscopist

Eckert & Ziegler
Analytics

1380 Seaboard Industrial Blvd.
Atlanta, Georgia 30318
Tel 404·352·8677
Fax 404·352·2837
www.ezag.com

CERTIFICATE OF CALIBRATION
Standard Reference Source

SRS Number: 108401A
Source Description: High Density Solid in Polyethylene Cylinder Filled to Capacity
Product Code: 8403-EG-SDHD
Customer: Georgia Institute of Technology
P.O. Number: 2500443296, Item 1

This standard radionuclide source was prepared from an aliquot measured gravimetrically from a master radionuclide solution calibrated with a germanium gamma-ray spectrometer system. Additional radionuclides were added gravimetrically from solutions calibrated by gamma-ray spectrometry, ionization chamber, or liquid scintillation counting. Calibration and purity were checked using germanium gamma-ray spectrometry. At the time of calibration no interfering gamma-ray emitting impurities were detected. The gamma-ray emission rates for the most intense gamma-ray lines are given. Eckert & Ziegler Analytics (EZA) maintains traceability to the National Institute of Standards and Technology (NIST) through a Measurements Assurance Program as described in USNRC Regulatory Guide 4.15, Revision 2, July 2007, and compliance with ANSI N42.22-1995, "Traceability of Radioactive Sources to NIST."

Density of solid matrix: 1.70 g/cm³ ± 3 %.

Reference Date: 01-January-2018 12:00 PM EST
MGS Mixture

Isotope	Gamma-Ray Energy, keV	Half-Life, d	Activity, Bq	Flux, s^{-1}	Uncertainty u_A, %	Uncertainty u_B, %	Uncertainty U, %*	Calibration Method**
Pb-210	46.5	8.109E+03	1.450E+04	6.163E+02	0.1	2.1	4.2	4π LS
Am-241	59.5	1.580E+05	1.162E+03	4.172E+02	0.1	1.8	3.6	4π LS
Cd-109	88.0	4.614E+02	1.610E+04	5.955E+02	0.5	2.0	4.1	HPGe
Co-57	122.1	2.717E+02	3.654E+02	3.128E+02	0.4	1.7	3.4	HPGe
Ce-139	165.9	1.376E+02	5.499E+02	4.399E+02	0.4	1.7	3.6	HPGe
Hg-203	279.2	4.659E+01	1.185E+03	9.665E+02	0.3	1.7	3.5	HPGe
Sn-113	391.7	1.151E+02	9.407E+02	6.112E+02	0.4	1.9	3.9	HPGe
Cs-137	661.7	1.099E+04	4.612E+02	3.925E+02	0.7	1.9	4.1	HPGe
Y-88	898.0	1.066E+02	1.577E+03	1.478E+03	0.7	1.7	3.7	HPGe
Y-88	1836.1	———	———	1.565E+03	0.7	1.7	3.7	———
Co-60	1173.2	1.925E+03	7.219E+02	7.208E+02	0.7	1.8	3.9	HPGe
Co-60	1332.5	———	———	7.217E+02	0.7	1.8	3.9	———

Mixed Gamma (MGS) master solution is EZA's eight isotope mixture which is calibrated quarterly and consists of Cd-109, Co-57, Ce-139, Hg-203, Sn-113, Cs-137, Y-88, and Co-60. ***Uncertainty:** U - Relative expanded uncertainty, k = 2. See NIST Technical Note 1297, "Guidelines for Evaluating and Expressing the Uncertainty of NIST Measurement Results." ****Calibration Methods:** 4π LS - 4π Liquid Scintillation Counting, HPGe - High Purity Germanium Gamma-Ray Spectrometer, IC - Ionization Chamber.

(Certificate continued on reverse side)

B.4 Inorganic Ventures Certificate for 10 ppm Au/HCl solution

INORGANIC VENTURES
300 Technology Drive
Christiansburg, VA 24073 · USA
inorganicventures.com

CERTIFICATE OF ANALYSIS

tel: 800.669.6799 · 540.585.3030
fax: 540.585.3012
info@inorganicventures.com

1.0 ACCREDITATION / REGISTRATION

INORGANIC VENTURES is accredited to ISO 17034, "General Requirements for the Competence of Reference Material Producers" and ISO/IEC 17025, "General Requirements for the Competence of Testing and Calibration Laboratories". Inorganic Ventures is also an ISO 9001 registered manufacturer (QSR Certificate Number QSR-1034).

ACCREDITED Testing Laboratory Certificate 883.01
ACCREDITED Reference Material Producer Certificate 883.02

2.0 PRODUCT DESCRIPTION

Product Code:	Single Analyte Mass Spec Solution
Catalog Number:	MSAU-10PPM
Lot Number:	P2-AU681002
Matrix:	10% (v/v) HCl
Value / Analyte(s):	10 µg/mL ea: Gold
Starting Material:	Gold trichloride
Starting Material Lot#:	2213
Starting Material Purity:	99.9930%

3.0 CERTIFIED VALUES AND UNCERTAINTIES

Certified Value: 9.999 ± 0.055 µg/mL

Density: 1.020 g/mL (measured at 20 ± 4 °C)

Assay Information:

ANALYTE	METHOD	NIST SRM#	SRM LOT#
Au	ICP Assay	3121	991806
Au	Calculated		See Sec. 4.2

The following equations are used in the calculation of the certified value and the uncertainty. Reported uncertainties represent expanded uncertainties expressed at approximately the 95% confidence level using a coverage factor of k = 2.

Characterization of CRM/RM by Two or More Methods

Certified Value, $X_{CRM/RM}$, where two or more methods of characterization are used is the weighted mean of the results:

$X_{CRM/RM} = \Sigma(w_i)(X_i)$

X_i = mean of Assay Method i with standard uncertainty $u_{char\ i}$

w_i = the weighting factors for each method calculated using the inverse square of the variance:

$w_i = (1/u_{char\ i})^2 / (\Sigma(1/(u_{char\ j})^2)$

CRM/RM Expanded Uncertainty (±) = $U_{CRM/RM} = k\,(u^2_{char} + u^2_{bb} + u^2_{lts} + u^2_{ts})^{1/2}$

k = coverage factor = 2

$u_{char} = [\Sigma((w_i)^2 (u_{char\ j})^2)]^{1/2}$ where $u_{char\ i}$ are the errors from each characterization method

u_{bb} = bottle to bottle homogeneity standard uncertainty

u_{lts} = long term stability standard uncertainty (storage)

u_{ts} = transport stability standard uncertainty

Characterization of CRM/RM by One Method

Certified Value, $X_{CRM/RM}$, where one method of characterization is used is the mean of individual results:

$X_{CRM/RM} = (X_a)\ (u_{char\ a})$

X_a = mean of Assay Method A with

$u_{char\ a}$ = the standard uncertainty of characterization Method A

CRM/RM Expanded Uncertainty (±) = $U_{CRM/RM} = k\,(u^2_{char\ a} + u^2_{bb} + u^2_{lts} + u^2_{ts})^{1/2}$

k = coverage factor = 2

$u_{char\ a}$ = the errors from characterization

u_{bb} = bottle to bottle homogeneity standard uncertainty

u_{lts} = long term stability standard uncertainty (storage)

u_{ts} = transport stability standard uncertainty

4.0 TRACEABILITY TO NIST

- This product is traceable to NIST via an unbroken chain of comparisons. The uncertainties for each certified value are reported, taking into account the SRM/RM uncertainty error and the measurement, weighing and volume dilution errors. In rare cases where no NIST SRM/RM are available, the term 'in-house std.' is specified.

B.5 Gold powder certificate

Alfa Aesar

Certificate of analysis

Product No.: 00765

Product: Gold powder, spherical, <5 micron, 99.95% (metals basis)

Lot No.: Z13E025

Average particle diameter	1.5 µm
Specific surface area	0.23 m^2/g
Tap density	8.3 g/ml
Gold	99.98 %
Chloride	< 0.001 %
Loss at 110 ºC in air	0.02 %
Loss at 538 ºC in air	0.10 %
Particle size:	
< D5	< 0.7 µm
< D10	< 0.9 µm
< D50	< 1.9 µm
< D90	< 3.5 µm
< D95	< 4.4 µm

Ag	0.0006	Al	ND
Ba	ND	Bi	ND
Ca	ND	Cd	ND
Cu	ND	Fe	ND
K	ND	Li	ND
Mg	ND	Mn	ND
Na	ND	Ni	ND
Pb	ND	Pd	ND
Pt	ND	Rh	ND
Ru	ND	Sb	ND
Si	ND	Sn	ND
Zn	ND		

Values are given in percent unless otherwise specified
ND: Not detected

This document has been electronically generated and does not require a signature.

Order our products online **www.alfa.com**

ThermoFisher SCIENTIFIC

B.6 Wheaton Socorex Calibra Performance Data

PERFORMANCE DATA AND ORDERING INFORMATION | **TECHNISCHE DATEN UND BESTELLINFORMATION** | **DONNÉES TECHNIQUES ET CATALOGUE**

Cat. No. Kat. Nr. No. Cat.	Capacity Volumen Volume mL	Division Teilung Division mL	Accuracy (mean error%)* Richtigkeit (R%) Justesse (err. rel.%) Min. vol.	Accuracy (mean error%)* Max. vol.	Precision (CV%)* Präzision (CV%) Précision (CV%) Min. vol.	Precision (CV%)* Max. vol.
832.02	0,2 – 2 mL	0,01 mL (10 µL)	< ± 1,5%	< ± 0,5%	< 0,5%	< 0,2%
832.10	1 – 10 mL	0,1 mL (100 µL)	< ± 1,5%	< ± 0,5%	< 0,3%	< 0,15%

Cat. No. Kat. Nr. No. Cat.	Tips Spitzen Embouts	Cat. No. Kat. Nr. No. Cat.	Nozzle filters Schutzfilter Filtres de protection
312.02	Macrotip 2 mL 2 × 250/bag	322.02	For 2 mL model 250/bag
313.02	Pasteur pipette 2 mL, ext. ∅ 6,5 – 7,2 mm 250/pack		
312.10	Macrotip 10 mL 3 × 100/bag	322.10	For 10 mL model 100/bag

* *Values obtained with forward pipetting mode, at constant temperature (+/–0,5°C) comprised between 20 and 25°C with Aqua bidest according to EN ISO 8655 / DIN 12650 part 6. Viscous or volatile liquids may generate deviations greater than shown in above figures.*

* *Diese Werte wurden mit Normal Pipettiervorgang, bei einer konstanten Raumtemperatur (+/–0.5°C) zwischen 20 und 25°C mit destilliertem Wasser erreicht, gemäss EN ISO 8655 / DIN 12650, Teil 6. Hochviskose oder entspannte Flüssigkeiten können zu Resultaten führen, die den oben aufgeführten Daten nicht genau entsprechen.*

* *Valeurs obtenues en mode de pipettage direct, avec de l'eau distillée à une température ambiante constante (+/–0,5°C) comprise entre 20 et 25°C selon la normeEN ISO 8655 / DIN 12650 section 6. Le pipettage de solutions visqueuses et hautement volatiles peut conduire à des déviations plus importantes que celles mentionnées ci-dessus.*

B.7 Mettler Toledo Conformity

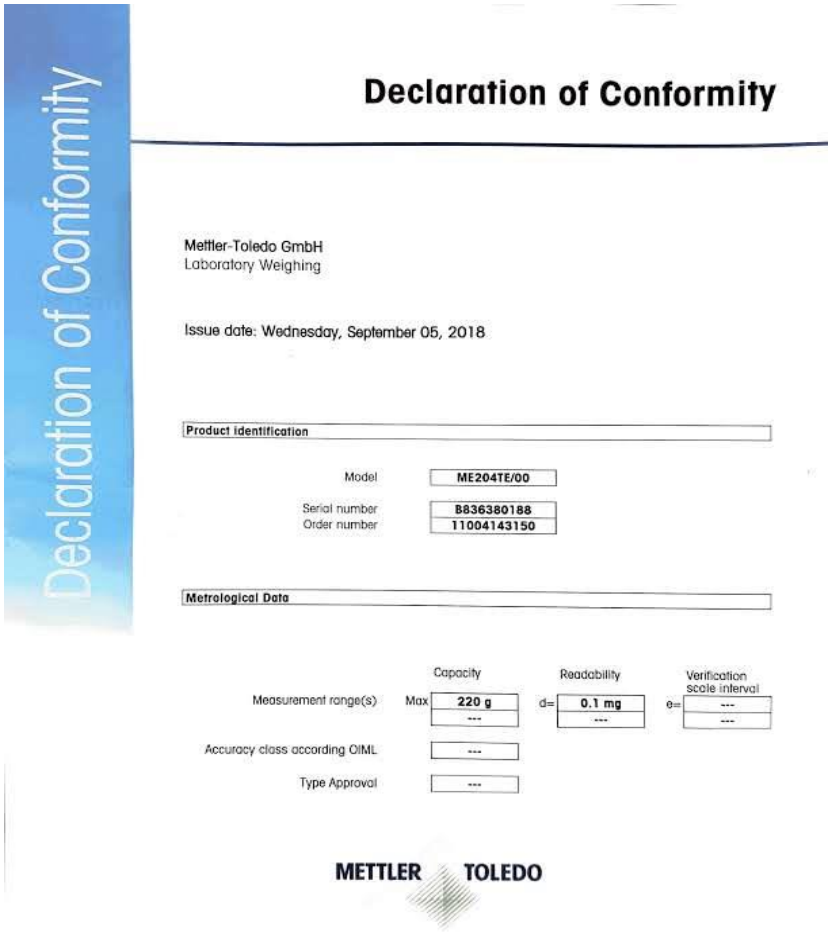

Declaration of Conformity

Declaration of Conformity

Mettler-Toledo GmbH
Laboratory Weighing

Issue date: Wednesday, September 05, 2018

Product identification

Model	ME204TE/00
Serial number	B836380188
Order number	11004143150

Metrological Data

	Capacity	Readability	Verification scale interval
Measurement range(s)	Max 220 g	d= 0.1 mg	e= ---
	---	---	---
Accuracy class according OIML	---		
Type Approval	---		

METTLER TOLEDO

REFERENCES

Alssabbaga, Moayyad, Abd Aziz Tajuddin, Mahayuddin Abdulmanapa, and Rafidah Zainona. 2017. "Evaluation of 3D printing materials for fabrication of a novel multifunctional." *Radiation Physics and Chemistry* 106-112.

2013. "Mixing." In *Food Process Engineering and Technology*, by Zeki Berk, 193-216. San Diego: Elsiver Science and Technology.

Brookhaven Nation Research Laboratory . n.d. *NuDat 2.7*. Accessed June 9th, 2019. https://www.nndc.bnl.gov/nudat2/.

Cabal, F P, N Lopez-Pino, Bernal-Castillo J L, Y M Martinez-Palenzuela, J Aguilar-Mena, K D'Alessandro, Y Arbelo, Y Corrales, and O Diaz. 2010. "Monte Carlo based geometrical model for efficiency calculation of an n-type HPGe detector." *Appliedl Radiation and Isotopes* 68, 2403-2408.

Canberaa Industries Inc. 2006. *Genie 2000 Operations Manual*. Meriden, CT.

Cao, L, J Jarrel, S White, K Herminghuysen, A Kauffman, D E Hardtmayer, J Sanders, and S Li. 2019. "A radioactive tracer dilution method to determine the mass of molten salt." *J Radioanal Nucl Chem* 314:387-33.

Ceh, Justin, Tom Youd, Zach Mastrovich, Cody Peterson, Sarah Khan, and Todd A Sasser. 2017. "Bismuth Infusion of ABS Enables Additive Manufacturing of Complex Radiological Phantoms." *Sensors* Vol 17 Iss 3.

GSU Physics Dept. n.d. *Densities of Common Substances.* Accessed July 8th, 2019. http://hyperphysics.phy-astr.gsu.edu/hbase/Tables/density.html.

Guest, P G. 1961. "The Solid Angle Subtended by a Cylinder." *Review of Scientific Instruments* 32, 164.

Hull, C W. 1986. Apparatus for production of three-dimensional objects by stereolithography. Patent US Patent 4575330.

Hull, Charles W. 1984. United States Patent 4,575,330.

Inorganic Ventures Inc. n.d. *100 ppm (µg/mL) Gold for ICP-MS - MSAU-100PPM-125ML.* Accessed June 13th, 2019. https://www.inorganicventures.com/productdisplay/100-ppm-gold-icp-ms-0.

Jacobs, P.F. 1992. *Rapid Prototyping & Manufacturing: Fundimentals of StereoLithography.* Society of Manufacturing Engineers.

Kice, John L. 1954. "Inhibition of polymerization of Methyl Methacrylate." *J. Am. Chem. Soc.,* July 8th: 6274 Vol. 76.

Knoll, G. F. 2010. *Radiation Detection and Measurement.* Hoboken, NJ: John Wiley & Sons.

Kodama, H. 1981. "Automatic method for fabricating a three-dimensional plastic model with photo-hardening polymer." *Review of Scientific Instruments* 1770–1773.

Ku, H. H. 1966. "Notes on the Use of Propagation of Error Formulas." *J of Res Natl Bureau of Standards* Vol. 70C No.4 263-273.

Lacey, P M C. 1954. "Developments in the theory of particle mixing." *Journal of Applied Chemistry* 257-268.

Leary M, Kron T, Keller C, Franich R, Lonski P. 2015. "Additive manufacture of custom radiation dosimetry phantoms: An automated method compatible with commercial polymer 3D printers." *Materials and Design* 86, 487-499.

Lowden, R A, S D Nunn, Kiggans J O Jr, and C D Bryan. 2015. *Powder Metallurgy Fabrication of Molybdenum Accelerator Target Disks.* Oak Ridge National Laboratory.

MakerBot Industries LLC. 2019. *https://www.thingiverse.com/.* Accessed June 6, 2019. https://www.thingiverse.com/.

Mirion Technologies Inc. 2019. "Spectrum Analysis." *Nuclear Measurement Principles.* Accessed Jul 14, 2019. http://www.canberra.com/literature/fundamental-principles/pdf/Spectrum-Analysis.pdf.

Ngo, Tuan D, Alireza Kashani, Gabriele Imbalzanoa, Kate T Q Nguyena, and David Huib. 2018. "Additive manufacturing (3D printing): A review of materials, methods, applications and challenges." *Composites Part B* 172-196.

Nienow, A W. 1997. "The suspension of solid particles." In *Mixing in Process Industries*, by N Harnby, M F Edwards and A W and Nienow, 364-393. Boston: Butterworth-Heinemann.

Nir-El, Y. 2013. "Correction for decay of during counting in gamma spectrometry." *Radiation Protection Dosimetry* Vol. 153, No. 3, 400-401.

Peters, D C. 1997. "Dynamics of emulsification." In *Mixing in Process Industries*, by N Harnby, M. F Edwards and A. W Nienow, 294-321. Boston: Butterworth-Heinemann.

Shaffer, Steven, Kejia Yang b, Vargas d Juan, Matthew A Di Prima, and Walter Voit. 2014. "On reducing anisotropy in 3D printed polymers via ionizing radiation." *Polymer* 55, 5969-5979.

SpecialChem. n.d. *PMMA or Acrylic: Guide to Support Your Future 'Transparent' Developments.* Accessed 6 12, 2019. https://omnexus.specialchem.com/selection-guide/polymethyl-methacrylate-pmma-acrylic-plastic.

Strauss, Michael G, Irvin S Sherman, Mark J Cattelino, Raul Brenner, and Richard H Pehl. 1977. "Intrinsic efficiency of germanium - a basis for calculating expected detector efficiency." *IEEE Transactions on Nuclear Science* Vol.24(1), pp.88-92.

Tavernier, S. 2010. *Experimental Techniques in Nuclear and Particles Physics.* Berlin: Springer Hiedelberg.

2018. "The Ultimate Guide to Stereolithographic 3D printing." *Formlabs.* Accessed January 19, 2019. https://formlabs.com/resources/.

Tyrka, Stanislaw. 1999. "A method for calculating the average solid angle subtended by a circular disk from uniformly distributed points within a coaxial circular plane." *Review of Scientific Instruments* 70, 3915.